Shuai He, Ching-Tai Ng

Guided wave-based identification of multiple cracks in beams using a Bayesian approach

Mechanical Systems and Signal Processing, 2017; 84(A):324-345

Guided wave-based identification of multiple cracks in beams using a Bayesian approach

Shuai He and Ching-Tai Ng*

School of Civil, Environmental & Mining Engineering, The University of Adelaide, Adelaide, SA 5005, Australia

Abstract

A guided wave damage identification method using a model-based approach is proposed to identify multiple cracks in beam-like structures. The guided wave propagation is simulated using spectral finite element method and a crack element is proposed to take into account the mode conversion effect. The Bayesian model class selection algorithm is employed to determine the crack number and then the Bayesian statistical framework is used to identify the crack parameters and the associated uncertainties. In order to improve the efficiency and ensure the reliability of identification, the Transitional Markov Chain Monte Carlo (TMCMC) method is implemented in the Bayesian approach. A series of numerical studies are carried out to assess the performance of the proposed method, in which the sensitivity of different guided wave modes and effect of different levels of measurement noise in identifying different numbers of cracks is studied in detail. The proposed method is also experimentally verified using guided wave data obtained from laser vibrometer. The results show that the proposed method is able to accurately identify the number, locations and sizes of the cracks, and also quantify the associated uncertainties. In

*Corresponding Author: Ching-Tai Ng (Email: alex.ng@adelaide.edu.au)

addition the proposed method is robust under measurement noise and different situations of the cracks.

Keywords: Multiple cracks; Damage identification; Bayesian statistical framework; Bayesian model class selection; Guided waves; Spectral finite element; Mode conversion

1 Introduction

1.1 Structural Health monitoring

Structural health monitoring (SHM) has attracted much attention as it plays a vital role in ensuring safety, reliability and serviceability of a range of infrastructures in civil, mechanical and aviation engineering. It provides a tool to continuously examine the integrity of structures and presents essential information of any damage and deterioration at the early stage. Numerous damage detection techniques have been developed to provide safety inspection for structures in the field of SHM. Conventional non-destructive evaluation (NDE) techniques are generally limited in measuring a very small region of the structure and not applicable to inspect inaccessible locations. Efficient damage inspection requires the pre-knowledge of possible damage locations, which is usually not available in practical situation for NDE. Acoustic emission [1] is a passive technique that is able to monitor the generation and growth of defects but it is not applicable to detect existing defects. The vibration-based techniques [2] have the capability to detect and locate the damage in entire structures. However, they are insensitive to incipient defects as they are based on low vibrational frequency.

1.2 GW Damage identification

Guided wave (GW) has been proven sensitive to small and various types of damages [3][4]. GW is a mechanical stress wave, which can be actuated by piezoelectric transducers installed on structures and its propagation is confined to the structures guided by structural boundaries. It can be used to inspect large area of the structures as it is able to propagate a long distance. In recent years, GW has demonstrated significant capabilities in damage detection [5] in a variety of structural components, which are commonly categorised into one- (1D) and two-dimensional (2D) waveguides. The

characteristics of GW propagation and its interaction with damage have been studied for 1D waveguides (e.g. pipes [6]) and beams [7][8] and 2D waveguides (e.g. plates [9]).

Based on the identified damage information, the damage detection process has four different levels, i.e. determine i) damage existence, ii) damage location, iii) damage severity and iv) remaining service lifespan of structures prediction [10]. In the literature different types of damage detection techniques have been developed for 2D waveguide and most of them are able to identify the existence, location and severity of the damages. For example, numerous advance damage detection techniques, such as damage imaging [11][12], maximum-likelihood estimation [13], diffraction tomography [14][15], phased-array beamforming [16], model based approach [17][18] and the Bayesian interface [19][20] were developed for plate-like structures. In contrast, most GW based damage detection techniques for 1D waveguides were limited in identifying the existence and location of damage [21].

1.3 Model-based approaches

There are two major approaches in GW damage detection of 1D waveguides: the non-model and model based approaches. Most research of GW damage identification focuses on non-model based approaches. Generally, non-model based approaches apply forward algorithm to detect damage by recognising the subsequent changes in certain features between the damaged and healthy state of structures. However, accurate baseline signal is difficult to obtain because it normally contains numerous unnecessary data, such as noise from environments, natural vibration of the structures and data acquisition systems. Although different signal processing techniques have been recently proposed to extract the damage information in the measured signal, these studies only

roughly quantified the severity of the damage. For example, Hossein Abadi *et al*. [22] proposed a pattern recognise technique to detect step damage on a thick steel beam based on discrete wavelet transform of GW signal. Experimental results demonstrated that the damage location was appropriately detected and its depth was estimated. Amjad *et al*. [23] utilized the changes in time-of-flight and phase to detect circular hole-type damage in 1D waveguide. Different signal processing techniques such as Fast Fourier Transform (FFT), Wigner-Ville Distribution Transform (WVDT), S-Transform (ST) and Hilbert Huang Transform (HHT) were employed to improve the quality of the GW signal in identifying the damage size.

Model-based approach is capable to characterise more complicated damage by updating a damage model. The damage parameters, such as damage location and geometry, are treated as unknown parameters and updated through minimising the discrepancy between the simulated and measured data. This approach is able to provide more quantitative information in the damage identification, and hence, this paper focuses on using the GW model-based approach for cracks identification of beam-like structures.

1.4 Modelling of GW propagation and scattering

Methods of modelling the GW propagation can be found in the literature [24]. Generally, GW propagation could be numerically modelled by conventional finite element (FE) method [25], while this method is impractical for model-based damage identification. The mesh size of the FE element usually needs to be small enough to ensure the accuracy in simulating the GW propagation but it is computational expensive. Other numerical methods, such as finite difference method [26], would

confront convergence problem when the GW propagates through different materials. Finite strip element method [27] is difficult to be applied to geometry-complex structures. Boundary element method [28] is inefficient for simulating large structures. The frequency-domain spectral finite element (SFE) method has been widely applied in most GW model-based damage detection techniques [7][29][30] because of its computational efficiency. It has been used for damage identification, for example, based on genetic algorithm (GA) in beam-like structure with a symmetric open crack [29] and in composite beams with delamination [30], and Bayesian statistical framework combined with simulating annealing (SA) [31] and particle swarm optimization (PSO) algorithm [7] in a beam with a step damage. However, because the frequency-domain SFE method requires one side of the structure to be infinitely long, it is unsuitable for modelling practical and complex structures.

Time-domain SFE method, which is also called the p-version FEM [32], has the same flexibility in model discretisation as conventional FEM. The method uses high-order approximation polynomials to reduce the number of elements. Also, the application of Gauss-Lobatto-Legendre (GLL) nodes, leads to a diagonal mass matrix, and hence, the dynamic equilibrium of the model can be solved efficiently by explicit central difference method. In addition, the Runge effect is avoided by the application of this GLL-node element [33]. The time-domain SFE modelling has been proven to be an effective tool in simulating GW propagation for 1D and 2D waveguides [34]. In this paper, the time-domain SFE method is utilised to simulate both fundamental longitudinal (S_0) and flexural (A_0) GWs propagation based on the Mindlin-Herrmann rod [35] and Timoshenko beam theory [36], respectively. These theories provide more accurate results for the high frequency GW propagation.

GW mode-conversion effect is a general phenomenon occurring at the moment when the GW interacts with asymmetric discontinuity in the waveguide. Additional damage information from the mode-converted GW can be provided to describe the damage features. In the literatures, for example, Xu *et al*. [37] determined the depth of a partial-thickness crack in plate by the mode converted energy rate using FE simulation. Li *et al*. [38] compared the mode-converted signal with the baseline signal to detect damage in high-speed railway. However, the use of GW mode-conversion effect for model-based damage identification in beam-like structures has not been studied. In this paper, a time-domain SFE cracked beam element [39] was adapted to simulate the mode-conversion effect. The flexibility of the cracked element was formed by applying the Castigliano's theorem and laws of fracture mechanics to couple the longitudinal and flexural displacement. As a result, the mode converted GW signal was simulated and better performance of damage characterisation in beam-like structure was achieved.

1.5 Bayesian approach

Bayesian statistical framework was initially applied in the field of low-frequency vibrational test [40]. It was then extended to the GW model-based crack identification in beam-like structures [7], [29]-[31]. This method determines the damage parameters using the maximum likelihood method and provides the quantification of the corresponding uncertainties, which is significantly useful for planning the restoration work in engineering practice. However, most of the studies were limited to identify single damage in 1D waveguides. This is because in multiple-damage situation, a numerical model that considers the number of damage more than the actual damage number will always have better fitting between the simulated and measured data in the presence of measurement noise and modelling error. Therefore, the selection of the

model with a pre-defined damage number based solely on the fitting between the modelled and measured data can be very misleading. In order to solve this problem, the Bayesian model class selection algorithm [41][42] was employed to identify the number of cracks for multiple-damage situation in this paper, which considers a penalty against the model complexity, i.e. increasing number of cracks.

Crack identification in model-based approach requires determine the optimal crack parameters that minimises the discrepancy between the simulated data of the crack model and measured data. In the case of single crack identification, which is usually treated as an identifiable situation [41], there is one or limited number of optimal crack parameter regions in the parameter space. Identification of the crack is equivalent to finding the global optimum by using global optimisation algorithms such as GA, SA and PSO. While in the case of multi-crack identification, the problem is possible to be unidentifiable [41] and the aforementioned optimisation tools are inapplicable. In order to solve this difficulty, this paper utilises Bayesian approach with implementation of the transitional Markov Chain Monte Carlo (TMCMC) sampling method [43] to identify the number of cracks and the optimal crack parameters

The arrangement of the paper is listed as follow. The time-domain SFE method and a proposed SFE crack model are presented in Section 2. The Bayesian model class selection and Bayesian statistical framework for damage identification are then described in Section 3. Section 4 describes the TMCMC algorithm. After that a series of numerical case studies for investigating the reliability and computational efficiency of the TMCMC algorithm are presented in Section 5. Different GW modes, crack numbers, noise levels and measurement locations are considered in the numerical case studies. In addition, the results of experimental case studies are presented to verify the

practicability of this approach in Section 6. Finally, conclusions are drawn in Section 7.

2 Time-domain spectral finite element method

2.1 Mindlin-Herrmann and Timoshenko beam theory

It has been experimentally proven that the Mindlin-Herrmann rod theory provides better results than the elementary rod theory in simulating the fundamental longitudinal GW propagation [44] while the Timoshenko beam theory performs better than the Euler–Bernoulli beam theory in simulating the fundamental flexural GW [21]. Although Love theory provides similar results to the Mindlin-Herrmann rod theory for low frequency (i.e., fundamental mode) GW propagation in thin rods, it changes the diagonal form of the mass matrix by introducing the lateral deformation component [21]. So it is inefficiency in solving the dynamic equilibrium using central difference method. Furthermore, Love theory is not sufficient to simulate the GW propagation in deep rods or at high frequency. Hence, the Mindlin-Herrmann rod theory and Timoshenko beam theory are chosen to model the GW propagation in this study.

[Figure 1. Distribution of GLL nodes and shape function of first four nodes (1^{st} node: solid line; 2^{nd} node: dashed line; 3^{rd} node: dotted line; 4^{th} node: dotted-dashed line)]

In the Mindlin-Herrmann rod theory, the longitudinal displacement $u(x)$ is coupled with an independent lateral contraction $\psi(x)$ that used to account for the Poisson effect [35]. In the Timoshenko beam theory, the effect of shear deformation is considered and the vertical displacement $v(x)$ is independent from the rotational function $\varphi(x)$. Thus, as shown in Figure 1, four degree-of-freedoms (DoFs) were considered at each node and eight nodes were employed to model a SFE beam element

in this paper. The displacement fields in the beam have the following forms:

$$\bar{u}(x,y) \approx u(x) - y\varphi(x) \quad \text{and} \quad \bar{v}(x,y) \approx \psi(x)y + v(x) \tag{1}$$

where y is the vertical distance from neutral axis. The governing equations of GWs using Mindlin-Herrmann rod theory and Timoshenko beam theory are defined as [21],[36]

$$\begin{aligned} \frac{2GA}{1-\nu}\left(\frac{\partial^2 u}{\partial x^2} + \nu\frac{\partial \psi}{\partial x}\right) &= \rho A\ddot{u} - F_l(x,t) \\ K_1^M GI\frac{\partial^2 \psi}{\partial x^2} - \frac{2GA}{1-\nu}\left(\nu\frac{\partial u}{\partial x} + \psi\right) &= K_2^M \rho I\ddot{\psi} \end{aligned} \tag{2}$$

$$\begin{aligned} K_1^T GA\frac{\partial}{\partial x}\left(\frac{\partial v}{\partial x} - \varphi\right) &= \rho A\ddot{v} - F_v(x,t) \\ EI\frac{\partial^2 \varphi}{\partial x^2} + K_1^T GA\left(\frac{\partial v}{\partial x} - \varphi\right) &= K_2^T \rho I\ddot{\varphi} \end{aligned} \tag{3}$$

where E and G are the Young's and shear modules. A denotes the cross-section area of the beam and I is the moment of inertia. ν and ρ are Poisson's ratio and mass density of the material, respectively. The external longitudinal and vertical excitation are illustrated by $F_l(x,t)$ and $F_v(x,t)$, which are the function of time *t* and location variable x, respectively. K_1^M, K_2^M and K_1^T can be adjusted to give the best correspondence with the experimental results in the considered frequency range. In this study K_1^M = 1.1, K_2^M=3.1 and K_1^T=0.922 are obtained from the experimental results reported in this paper. $K_2^T = 12K_1^T/\pi^2$ to match the cut-off frequency with guided wave modes.

2.2 Spectral finite element formulation

The dynamic equilibrium of the model in time-domain can be represented using the following Equation [34]

$$\mathbf{M}\ddot{\mathbf{U}} + \mathbf{C}\dot{\mathbf{U}} + \mathbf{K}\mathbf{U} = \mathbf{F}(t) \tag{4}$$

where the global mass matrix, damping matrix and stiffness matrix are denoted by $\mathbf{M}$, $\mathbf{C}$ and $\mathbf{K}$, respectively. These global matrices can be obtained by assembling the local element matrices. The external excitation force vector $\mathbf{F}(t)$ is a function of time. $\mathbf{C}$ is the global damping matrix related to the mass matrix, which has the following form $\mathbf{C}=\eta\mathbf{M}$, and η is the damping coefficient. $\mathbf{U}$, $\dot{\mathbf{U}}$ and $\ddot{\mathbf{U}}$ are the vectors of displacement, velocity and acceleration, respectively. For an element of length L_e, the element matrices $\mathbf{M}^e$ and $\mathbf{K}^e$, and the column vector $\mathbf{F}^e$ can be obtained using the following equations

$$\mathbf{M}^e \approx \sum_{i=1}^{n} w_i \mathbf{S}_e(\xi_i)^T \mathbf{r}_e \mathbf{S}_e(\xi_i) \left| J(\xi_i) \right| \tag{5}$$

$$\mathbf{K}^e \approx \sum_{i=1}^{n} w_i \mathbf{B}_e(\xi_i)^T \mathbf{E}_e \mathbf{B}_e(\xi_i) \left| J(\xi_i) \right| \tag{6}$$

$$\mathbf{F}^e \approx \sum_{i=1}^{n} w_i \mathbf{S}_e(\xi_i)^T \mathbf{f}_e(\xi_i) \left| J(\xi_i) \right| \tag{7}$$

where n is the number of the GLL integration points in the element. $\mathbf{r}_e$ is the mass density matrix. $\mathbf{E}_e$ is the stress-stain matrix indicating the relationship between stress and strain. $\mathbf{f}_e(\xi_i)$ is the external excitation. $\mathbf{B}_e$ is the strain-displacement operator and is defined as

$$\mathbf{B}_e(\xi) = \mathbf{D}\mathbf{S}_e(\xi), \quad \textit{and} \quad J = \frac{\partial x}{\partial \xi} \tag{8}$$

where J is the Jacobian functions transferring the local coordinate to the global domain. $\mathbf{D}$ is the differential operator developed on the basis of Mindlin-Herrmann rod and Timoshenko beam theory, which are defined as

$$\mathbf{D}=\begin{bmatrix} \frac{\partial}{\partial x} & 0 & 0 & 0 \\ 0 & 1 & 0 & 0 \\ 0 & \frac{\partial}{\partial x} & 0 & 0 \\ 0 & 0 & \frac{\partial}{\partial x} & -1 \\ 0 & 0 & 0 & \frac{\partial}{\partial x} \end{bmatrix}=\begin{bmatrix} \frac{1}{J}\frac{\partial}{\partial \xi} & 0 & 0 & 0 \\ 0 & 1 & 0 & 0 \\ 0 & \frac{1}{J}\frac{\partial}{\partial \xi} & 0 & 0 \\ 0 & 0 & \frac{1}{J}\frac{\partial}{\partial \xi} & -1 \\ 0 & 0 & 0 & \frac{1}{J}\frac{\partial}{\partial \xi} \end{bmatrix} \tag{9}$$

$\xi_i \in [-1,1]$ for $i \in 1,...,n$ is the coordinates of the GLL integration points, which can be obtained as the roots of the equation below

$$\left(1-\xi^2\right)L'_{n-1}(\xi)=0 \tag{10}$$

where L'_{n-1} is the first derivative of the Legendre polynomial of degree $n-1$. In this study an eight-node element is used, and hence, $n=8$, as shown in Figure 1. The weights w_i in Equations (5) – (7) is accounted for node i and it has the expression [33]

$$w_i=\frac{2}{n(n-1)[L_{n-1}(\xi_i)]^2} \tag{11}$$

As four DoFs (i.e., longitudinal displacement u, lateral contraction ψ, vertical displacement v and rotation φ) are considered at a node, the shape function matrix $\mathbf{S}_e$ has the form

$$\mathbf{S}_e=\mathbf{S}\otimes\mathbf{I} \tag{12}$$

where $\mathbf{S}=[S_1(\xi),...,S_n(\xi)]$ is a row vector. ' $\otimes$ ' denotes the Kronecker product and $\mathbf{I}$ is a 4×4 identity matrix. The shape function $S_i(\xi)$ at node i that is defined as

$$S_i(\xi)=\prod_{m=1,m\neq i}^{n}\frac{\xi-\xi_m}{\xi_i-\xi_m} \quad \text{for} \quad i(i\in 1,2,...,n) \tag{13}$$

where n illustrates the number of GLL integration points in each element and m means the sequence of node. The shape function has the orthogonal property as

$$S_i\left(\xi_j\right)=\begin{cases}1, i=j\\ 0, i\neq j\end{cases} \text{ for } j(j\in 1,2,...,n) \text{ and } \sum_{i=1}^{n} S_i\left(\xi_j\right)=1 \tag{14}$$

This property is illustrated in Figure 1. With the value of this shape function, the global mass matrix $\mathbf{M}$ in Equation (4) can achieve a diagonal form. This contributes to an explicit expression of the integrating equation using central difference scheme, and hence, the dynamic equilibrium of the model can be efficiently calculated.

Based on the Mindlin-Herrmann rod and Timoshenko beam theory, the mass density matrix $\mathbf{r}_e$ in Equation (5) and the stress-strain matrix $\mathbf{E}_e$ in Equation (6) are denoted as below

$$\mathbf{r}_e=\begin{bmatrix}\rho A & 0 & 0 & 0\\ 0 & K_2^M\rho I & 0 & 0\\ 0 & 0 & \rho A & 0\\ 0 & 0 & 0 & K_2^T\rho I\end{bmatrix} \tag{15}$$

and

$$\mathbf{E}_e=\begin{bmatrix}\frac{EA}{1-\nu^2} & \frac{\nu EA}{1-\nu^2} & 0 & 0 & 0\\ \frac{\nu EA}{1-\nu^2} & \frac{EA}{1-\nu^2} & 0 & 0 & 0\\ 0 & 0 & K_1^M GI & 0 & 0\\ 0 & 0 & 0 & K_1^T GA & 0\\ 0 & 0 & 0 & 0 & EI\end{bmatrix} \tag{16}$$

Substituting $\mathbf{D}$, $\mathbf{r}_e$, $\mathbf{E}_e$ and $\mathbf{S}_e$ into Equations (5) – (7), and the element mass matrix $\mathbf{M}^e$, stiffness matrix $\mathbf{K}^e$ and external force matrix $\mathbf{F}^e$ can be obtained to constitute the global matrices $\mathbf{M}$, $\mathbf{C}$ and $\mathbf{K}$ in Equation (4).

2.3 Crack element modelling

A two-node spectral crack element with length l_c was developed to simulate the scattering of GW and mode-conversion effect when the GW encounters the crack. The crack element can be located continuously at any location L_c along the beam. A transverse surface crack, which has an elliptical shape representing a practical situation of the crack [45], is modelled in the crack element. The element has a very small length (i.e., 0.1 mm) in the longitudinal direction of the beam, thus, it can be treated as dimensionless in this direction. As a result, the value of the strain in the longitudinal direction is neglected, and hence, the corresponding axis contraction $\psi(x)$ in this crack element is considered zero. The geometric of crack element is shown in Figure 2. The elliptical crack has a cross section with width b_c and depth d_c, and it is modelled at the location x_c measured from the left end of the crack element.

[Figure 2. Schematic diagram of the crack element for simulating a part-through surface crack]

The element stiffness matrix $\mathbf{K}_e^c$ for the crack element proposed in [46] is modified to account coupling of the longitudinal, transverse and rotational displacement, and hence, it can simulate the mode conversion effect when the incident GW interacts at the crack. The element stiffness matrix $\mathbf{K}_e^c$ is defined as

$$\mathbf{K}_e^c = \mathbf{Y}\mathbf{Q}_f^{-1}\mathbf{Y}^T \tag{17}$$

where the position transformation matrix $\mathbf{Y}$ is a function of crack location and is

defined as

$$\mathbf{Y}^T = \begin{bmatrix} 1 & 0 & 0 & -1 & 0 & 0 \\ 0 & 1 & 0 & 0 & -1 & l_c \\ 0 & 0 & 1 & 0 & 0 & -1 \end{bmatrix} \tag{18}$$

$\mathbf{Q}_f$ is the flexibility matrix and is defined as

$$\mathbf{Q}_f = \begin{pmatrix} q_{11} & q_{12} & q_{13} \\ q_{21} & q_{22} & q_{23} \\ q_{31} & q_{32} & q_{33} \end{pmatrix} \tag{19}$$

with

$$q_{11} = \frac{l_c}{EA} + I_{c1}, \quad q_{22} = \left(\frac{\alpha_s l_c}{GA} + \frac{l_c^3}{3EA} \right) + \left(I_{c3} + x_c^2 I_{c4} \right), \quad q_{33} = \frac{l_c}{EI} + I_{c4},$$

$$q_{12} = q_{21} = x_c I_{c2}, \quad q_{13} = q_{31} = -I_{c2}, \quad q_{23} = q_{32} = -\frac{l_c^2}{2EI} - x_c I_{c4} \tag{20}$$

where $\alpha_s = 10(1+\nu)/(12+11\nu)$ is the shear coefficient rectangular cross-section of the beam.

$$I_{c1} = \frac{8\pi\kappa^2}{Eb^2h^2\left[1+1.464\kappa^{1.65}\right]} \int_0^{\bar{b}} \int_0^{\pi/2} \bar{b}^2 \sin^2\phi F_I^{\,2} d\phi d\bar{b}$$

$$I_{c2} = \frac{48\pi\kappa^2}{Eb^2h^3\left[1+1.464\kappa^{1.65}\right]} \int_0^{\bar{b}} \int_0^{\pi/2} \bar{b}^2 \sin^2\phi H F_I^{\,2} d\phi d\bar{b}$$

$$I_{c3} = \frac{8\alpha_s^2\pi\kappa^2}{Eb^2h^2} \int_0^{\bar{b}} \int_0^{\pi/2} \bar{b}^2 \sin^2\phi F_{II}^{\,2} d\phi d\bar{b}$$

$$I_{c4} = \frac{288\pi\kappa^2}{Eb^2h^4\left[1+1.464\kappa^{1.65}\right]} \int_0^{\bar{b}} \int_0^{\pi/2} \bar{b}^2 \sin^2\phi H^2 F_I^{\,2} d\phi d\bar{b} \tag{21}$$

where $\kappa = d_c/\bar{b}$ and $\bar{b} = b_c/2$. h is the thickness of the beam. F_I and F_{II} are the empirical boundary calibration factors accounted for tension [47] and shear [48] for the semielliptical surface crack, respectively. They are functions of crack depth d_c and

crack width b_c. The details of the F_I, F_{II} and H are summarised in Appendix A.

3 Bayesian approach for multiple cracks identification

In order to identify multiple cracks, the proposed Bayesian approach contains two stages. In stage-one the number of cracks (i.e., the most suitable model class) is determined using Bayesian model class selection method. The crack parameters are then identified using Bayesian statistical framework in stage-two.

3.1 Stage-one: Bayesian model class selection

In stage-one of the proposed methodology a series of model classes $\mathbf{M} \equiv \{M_j : j = 1, 2, ..., N_M\}$, which represent beams with different number of cracks, are considered. The procedure is shown in Figure 3.

[Figure 3. Framework of Bayesian model class selection]

Using the Bayesian model class selection method [41][42], the plausibility of the considered model classes can be assessed based on their posterior probability from the Bayes' Theorem, i.e. the probability of the model class conditional on the set of measurements D, as

$$P\left(M_j \middle| D, \mathbf{M}\right) = \frac{P\left(D \middle| M_j\right) P\left(M_j \middle| \mathbf{M}\right)}{\sum_{i=1}^{N_M} P\left(D \middle| M_i\right) P\left(M_i \middle| \mathbf{M}\right)} \tag{22}$$

where M_j denotes a model class with j cracks, $j = 1, ..., N_M$. N_M is the maximum number of cracks considered. $P\left(M_j \middle| \mathbf{M}\right)$ is the prior probability of the model class

M_j and $\sum_{j=1}^{N_M} P\left(M_j|\mathbf{M}\right)=1$. As there is no available prior information about the number of cracks, the prior probability $P\left(M_j|\mathbf{M}\right)$ is set to be $1/N_{M_j}$ for each model class in this study. The evaluation of $P(M_j \mid D,\mathbf{M})$ requires determination of the evidence $P\left(D|M_j\right)$, which can be expressed as

$$P\left(D|M_j\right)=\int P\left(D|\boldsymbol{\theta}_j,M_j\right)P\left(\boldsymbol{\theta}_j|M_j\right)d\boldsymbol{\theta}_j \tag{23}$$

where $\boldsymbol{\theta}_j$ is a vector containing the uncertain crack parameters, such as locations, widths and depths of the cracks, to be identified for the model class M_j (a beam with j cracks). However, Equation (23) involves a multi-dimensional integral, it is too complex to analytically integrate this equation. Laplace's method of asymptotic approximation can be used for model class that is globally identifiable. In multiple cracks identification, it involves model classes with different number of cracks from less than to more than the true number of cracks. For a given measured data, the model updating problem becomes unidentifiable when the model class (model class with more number of cracks) is too complex. In this situation, stochastic simulation methods, such as TMCMC [43] and Subset simulation methods [49][50][51], are practical for calculating the evidence value of theses model classes. In this paper, the TMCMC method will be used to calculate the evidence value in Equation (23) and the details will be discussed in Section 4.

In the Bayesian model class selection method, the penalty against complexity can be obtained by considering the evidence from an information-theoretic point of view, consider the log of the evidence as [52]

$$\ln\left[P\left(D\middle|M_j\right)\right]=\int\ln\left[\frac{P\left(D\middle|\boldsymbol{\theta}_j,M_j\right)P\left(\boldsymbol{\theta}_j\middle|M_j\right)}{P\left(\boldsymbol{\theta}_j\middle|D,M_j\right)}\right]P\left(\boldsymbol{\theta}_j\middle|D,M_j\right)d\boldsymbol{\theta}_j$$
$$=\int\ln\left[P\left(D\middle|\boldsymbol{\theta}_j,M_j\right)\right]P\left(\boldsymbol{\theta}_j\middle|D,M_j\right)d\boldsymbol{\theta}_j-\int\ln\left[\frac{P\left(\boldsymbol{\theta}_j\middle|D,M_j\right)}{P\left(\boldsymbol{\theta}_j\middle|M_j\right)}\right]P\left(\boldsymbol{\theta}_j\middle|D,M_j\right)d\boldsymbol{\theta}_j \tag{24}$$

The left side of Equation (24) is the log evidence of the model class M_j. It can be decomposed into two different terms on the right hand side of the equation. The first term is the log-likelihood function, which is a data-fit term, indicating the plausibility of the model class M_j. The model class with more number of cracks has larger log-likelihood value. The second term is relative entropy between the prior and posterior distribution, which is a measure of the information gained about $\boldsymbol{\theta}_j$ from the data D. It provides a penalty against more 'complex' model class, i.e. model class with more number of cracks in this study. Thus the log evidence $\ln[p(D|M_j)]$ automatically implements a quantitative Ockham's razor in term of a trade-off between a data-fit measure and a complexity measure for each model class. If the selection of the model class is based purely on the log-likelihood function, i.e. the data-fit term in Equation (24), then model class with more number of cracks will be preferred over model class with less number of cracks and this is the case for most of the damage detection methods based on the maximum likelihood approach or error minimisation approach. In Bayesian model class selection method, the model class with the maximum value of the log evidence value will be selected and this provides a robust identification of the number of cracks in the beams.

3.2 Stage-two: Bayesian approach for identifying crack parameters

The stage-two of the Bayesian approach is to determine the optimal value of the crack

parameters $\boldsymbol{\theta}_j$. Given a Bayesian model class M_j, the model response data D defined by the model parameters $\boldsymbol{\theta}_j$ can be used to update the corresponding plausibility of each model. The posterior probability density function (PDF) of uncertain crack parameters conditional on the measurement D and the model class M_j can be estimated as follows:

$$P\left(\boldsymbol{\theta}_j \middle| D, M_j\right) \propto P\left(D \middle| \boldsymbol{\theta}_j, M_j\right) P\left(\boldsymbol{\theta}_j \middle| M_j\right) \tag{25}$$

where $P\left(\boldsymbol{\theta}_j \middle| M_j\right)$ is the prior probability of the crack parameters based on the initial engineering judgement about the damage parameters. $P\left(D \middle| \boldsymbol{\theta}_j, M_j\right)$ is the likelihood function indicating the probability of getting the response data D based on the crack parameters $\boldsymbol{\theta}_j$. Based on the Principle of Maximum information Entropy [53], this paper assumes the likelihood function follows the Gaussian distribution with zero mean and standard deviation of prediction error σ_j as

$$P\left(D \middle| \boldsymbol{\theta}_j, M_j\right) = \frac{1}{\left(2\pi\sigma_j^2\right)^{\frac{N_t N_o}{2}}} \exp\left(-\frac{1}{2\sigma_j^2} \mathrm{J}\ \left(t; \boldsymbol{\theta}_j\right) \right) \tag{26}$$

where J is the goodness-of-fit function and is given as follows

$$\mathrm{J}\ \left(t; \boldsymbol{\theta}_j\right) = \sum_{o=1}^{N_o} \sum_{t=1}^{N_t} \left[q_m\left(t\right) - q\left(t; \boldsymbol{\theta}_j\right) \right]^2 \tag{27}$$

where $q_m\left(t\right)$ is the response displacement measured from experiment at t-th time step. $q\left(t; \boldsymbol{\theta}_j\right)$ is the simulated response displacement from the chosen model class M_j defined by the uncertain parameters $\boldsymbol{\theta}_j$. N_t and N_o denote the numbers of measurement time steps and the measured DoF, respectively. The variance of the prediction error σ_j^2 can be treated as an uncertain parameter in the analysis [43]. Since σ_j^2 is always positive, its prior distribution can be modelled by an inverse Gamma distribution, and hence, σ_j^2 can be sampled from $IG(0.5N_tN_o+1, 0.5\mathrm{J}\ (t; \boldsymbol{\theta}_j))$ [54]

where IG is the inverse Gamma distribution.

For identifiable cases, the posterior PDF in Equation (25) can be approximated by a multivariable Gaussian PDF based on the global optimal model parameter $\hat{\boldsymbol{\theta}}_j$ [40]. However, in multiple cracks identification cases, the problem may become unidentifiable for more complex model, i.e. model with more number of cracks. This make the multivariable Gaussian PDF cannot accurately approximate the posterior PDF. In this regard the Equation (25) is estimated alternatively using stochastic sampling method with a set of parameter samples $\boldsymbol{\theta}_j^{(h)}$, $h=1,...,N_s$, drawn from target distribution, where N_m is the number of samples at the m-th stage (final stage). In this paper the samples are drawn using the TMCMC sampler adapted from [43] and the details are described in the Section 4. At the final stage of TMCMC, the samples drawn from TMCMC sampler are asymptotically distributed as $P(D|\boldsymbol{\theta}_j, M_j)$, the identified crack parameters can be estimated by the sample means. The marginal posterior PDF of the i-th uncertain parameter can be obtained by adaptive kernel density estimation with Gaussian distribution being the kernel PDF [55][56] as

$$k\left(\boldsymbol{\theta}_j(i)\right)=\frac{1}{N_s}\sum_{h=1}^{N_s}W^{(h)}\mathrm{N}\left(\boldsymbol{\theta}_j^{(h)}(i),\mathbf{C}(i,i)\right) \tag{28}$$

where $\mathrm{N}(\mu,\Sigma)$ is the Gaussian distribution with mean μ and covariance matrix Σ. $W^{(h)}$ is the weighting of the h-th sample. $\mathbf{C}(i,i)$ is the i-th diagonal element of the sample covariance matrix calculated by the samples at the final stage of TMCMC. In details of the adaptive kernel density estimation can be found in [55][56].

4 Transitional Markov Chain Monte Carlo algorithm

Accurate estimation of the posterior PDF $P(D|\boldsymbol{\theta}_j, M_j)$ and evidence $P(D|M_j)$ requires samples drawn from the target distribution. In general samplers generate samples from prior PDF, which is quite different from the posterior PDF in an unidentifiable situation. In this aspect conventional Markov Chain Monte Carlo (MCMC) sampler is inefficient as a large number of samples will be rejected until it converges to the stable distribution of the samples. The TMCMC sampling method is more efficient than conventional MCMC as it generates samples from a series of stages, which gradually approximates the final PDF in Equation (24). Other sampling methods, such as Subset Simulation [49][50][51], also have been recently developed to address this problem and they are found to be robust regardless of the dimension of parameters. Since TMCMC has many successful applications, this study employs the TMCMC in the Bayesian approach. The schematic framework for TMCMC algorithm is shown in Figure 4.

[Figure 4. Framework of TMCMC algorithm]

In the beginning stage, the TMCMC sampler generates samples $\{\boldsymbol{\theta}_1^{(h)} : h = 1, ..., N_1\}$ for from the prior PDF where N_1 is the number of samples at $s = 1$ stage. The prior PDF is chosen based on engineering experience, and in this study a uniform distribution is employed. In step two the TMCMC sampler uses a series of intermediate stages $s = 2, \ldots, m$ to generate samples gradually converging to the PDF region with high probability. Specifically, the samples are generated twice at each stage. First, it generates samples from the transitional PDFs $P(D|M, \boldsymbol{\theta}_s^{(h)})^{T_{s+1}-T_s}$ using a resampling

technique. For example, given N_s samples $\{\boldsymbol{\theta}_s^{(h)}, h=1,\ldots,N_s\}$ generated from the previous stage, redraw N_k^r samples $\{\boldsymbol{\theta}_s^{(h),r}, h=1,\ldots,N_s\}$ from the N_s samples with the resampling probability $P_{re}(\boldsymbol{\theta}_s^{(h)}) = W(\boldsymbol{\theta}_s^{(h)}) \Big/ \sum_{h=1}^{N_s} W(\boldsymbol{\theta}_s^{(h)})$ for each sample. It should be noted that the same sample $\theta_s^{(h),r}$ can be drawn repeatedly and the repeating number of this sample is recorded as $R_s^{(h)}$. $W(\boldsymbol{\theta}_s^{(h)})$ is the 'plausibility weight' of each of the N_s samples and it has the following expression

$$W(\boldsymbol{\theta}_s^{(h)}) = \frac{P\left(\boldsymbol{\theta}_s^{(h)}|M_j\right) P\left(D|M_j, \boldsymbol{\theta}_s^{(h)}\right)^{T_{s+1}}}{P\left(\boldsymbol{\theta}_s^{(h)}|M_j\right) P\left(D|M_j, \boldsymbol{\theta}_s^{(h)}\right)^{T_s}} = P\left(D|M_j, \boldsymbol{\theta}_s^{(h)}\right)^{T_{s+1}-T_s}, h=1,\ldots,N_s \qquad (29)$$

and the intermediate PDF $P_s(\boldsymbol{\theta})$ in the stage s is expressed as

$$P_s(\boldsymbol{\theta}) \propto P\left(D|\boldsymbol{\theta}, M_j\right)^{T_s} P\left(\boldsymbol{\theta}|M_j\right),\ s=1,...,m \quad \text{and} \quad 0=T_1<T_2<\ldots<T_{\mathrm{m}}=1 \qquad (30)$$

where T_s is the temperature variable determining the smoothness of transition between two adjacent PDFs. If the T_s value increases slowly, more stages of resampling are applied. However, the convergence of the sampling is slow and more computational resources are required. The value of temperature variable T_s can be determined automatically in the TMCMC algorithm by setting the coefficient of variation (c.o.v.) of the 'plausibility weight' $W(\boldsymbol{\theta}_s^{(h)})$ at each stage s to a prescribed threshold, where the c.o.v. is the standard deviation of the sample vectors over their mean. It is found that 100% is a preferable choice for the prescribed threshold in usual case. As it can be seen from the Equation (29), each intermediate PDF is calculated interactively based on the PDF from last stage. This leads to the high performance of TMCMC in the high dimensional situation as the PDF converges gradually.

After the procedure of resampling, N_s^r MCMC chains are generated to draw N_{s+1} ($N_{s+1} = N_s$) new samples $\left\{\boldsymbol{\theta}_{s+1}^{(h)}, h = 1,\ldots, N_s\right\}$ from the next intermediate PDF $P_{s+1}(\boldsymbol{\theta})$. These chains start from each of the N_{s+1} samples $\{\boldsymbol{\theta}_s^{(h),r}, h = 1,\ldots, N_s\}$ and the sample number of each chain is $R_s^{(h)}$. The proposal samples are generated using Gaussian PDF with the covariance matrix $\sum_s$, which has the form

$$\sum_s = c_s^2 \sum_{h=1}^{N_s} w(\boldsymbol{\theta}_s^{(h)})(\boldsymbol{\theta}_s^{(h)} - \sum_{l=1}^{N_s} P_{re}(\boldsymbol{\theta}_s^{(h)})\boldsymbol{\theta}_s^{(l)})(\boldsymbol{\theta}_s^{(l)} - \sum_{l=1}^{N_s} P_{re}(\boldsymbol{\theta}_s^{(h)})\boldsymbol{\theta}_s^{(l)}) \tag{31}$$

where c_s is the step factor that influences the distance between samples in each Markov Chain at stage s. The accepting probability of each proposed sample $\boldsymbol{\theta}_{s+1}^{(h)}$ is $\left[P\left(D|\boldsymbol{\theta}_s^{(h)}, M_j\right) / P\left(D|\boldsymbol{\theta}_s^{(h)}, M_j\right)\right]^{T_{s+1}}$. Step two is repeated until the value of temperature T_{s+1} has reached 1, where concurrently the PDF has converged to the target PDF.

In the final stage (m -th stage), $\{\boldsymbol{\theta}_m^{(h)} : h = 1,..., N_m\}$ samples are asymptotically distributed as $P(D|\boldsymbol{\theta}_j, M_j)$ and evidence $p\left(D|M_j\right)$ of the model class M_j can be estimated using $S = \prod_{s=1}^{m}\left[\sum_{h=1}^{N_s} w(\boldsymbol{\theta}_s^{(h)}) \Big/ N_s\right]$. They are proven an asymptotically unbiased estimation [43]. Therefore, the crack number can be determined by comparing the model evidence of each model class.

5 Numerical case studies

The performance of the Bayesian multiple cracks identification method is studied in this section. This section has four subsections that focus on different scenarios, i.e., 1) GW

mode selection, 2) different crack numbers, 3) measurement noise levels and 4) cracked locations, as shown in Table 1. Aluminium beams with length 500 mm, depth 6 mm and width 12 mm were considered to investigate the capability of the proposed multiple crack identification method. The 3D explicit FE model was built based on the crack parameters described in Table 1 and the simulated signals were treated as synthetic experimental data.

The proposed time-domain SFE model described in Section 2 was used to model the GW propagation in the beams with cracks as described in Section 3. The uncertain crack parameters are the locations (L_c), depths (d_c) and widths (b_c) of the cracks. In the SFE model, 25 spectral elements with 8 GLL nodes were used for modelling the beam. The Young's module, density and Poisson's ratio of the beam are 70 GPa, 2700 kg/m^3 and 0.3, respectively. Damping was considered to obtain the same ratio between amplitude changes of GW response for simulated and experimental data [21] and the damping coefficient η was chosen at 550 s^{-1} in this paper. The interval Δt of each time step was 10^{-7} sec to guarantee a converged solution of the dynamic equilibrium Equation (4) solved by central difference method. The excitation signal is a 100 kHz narrow-band six-cycle sinusoidal tone burst pulse modulated by a Hanning window and it was applied to the left beam end to generate GW response. The response signal was calculated at the same location. In the FE model, the commercial software ABAQUS/Explicit v6.12-1 was used to simulate the synthetic experimental GW response. Eight-node 3D reduced integration solid brick elements (C3D8R) were used to model the cracked beam. The enhanced hourglass control was enabled for FE simulation and the mesh size are 0.4×0.4×0.4 mm^3 to ensure the numerical stability of GW simulation. The dynamic explicit solver, which applies the central difference scheme, was employed to solve the FE simulation of GW propagation. The time step

used in the SFE is 1×10^{-7} sec and the time step of the FE is automatically controlled by ABAQUS/Explicit. Measurement error was considered in the study and simulated by applying a percentage of root mean square (RMS) white noise the time-domain response of the GW calculated by the FE model.

The Bayesian statistical framework with TMCMC sampler was used to identify the crack parameters, i.e. locations, widths and depths of the cracks. Since the guided wave based crack identification focuses on early damage detection, it is assumed that the crack widths and depths are not larger than half of the width and depths of the beam cross-section. Thus the assignment of the prior PDF for θ_j is independently uniformly distributed over [0.02mm 0.48mm], [0mm 3mm] and [0mm 6mm] for crack locations, widths and depths, respectively. 500 samples were drawn at each stage in the TMCMC sampling. The threshold of the c.o.v. of the 'plausibility weight' $W(\boldsymbol{\theta}_s^{(h)})$ was chosen to be 100% and the step factor c_s was set as 0.1.

5.1 Selection of GW mode for damage identification

This section is to investigate the performance of S_0 and A_0 GW and the mode conversion effect in identifying the cracks. Two cracks were assumed in the aluminium beam and there are four cases, i.e., Case S1, S2, S3 and S4 as shown in Table 1. As the focus of this section is to determine the most suitable wave mode based on the accuracy and uncertainty of the identified crack parameters, we assumed the number of cracks is known, and hence, only the crack parameters are identified in this section.

The mode-conversion effect was studied first by comparing the identified crack parameters using the numerical model without (Case S1) and with (Case S1) considering the GW mode coupling effect. Specifically, two different time-domain SFE models were employed to simulate the response data. In the first model, the normal

cracked beam element without coupling the longitudinal and flexural displacement was employed. The second model with the proposed SFE cracked beam element was implemented to simulate the mode-coupled GW signals. In both cases, A_0 GW was excited and only the out-of-plane displacement was measured. The signal was normalised by the maximum absolute amplitude of the indecent wave. Table 2 shows the sample means and sample c.o.v.s of the uncertain crack parameters. The sample c.o.v. equals the ratio of the sample standard deviation to the sample mean. The value of the sample means indicate the identified crack parameters. The percentages of error of the identified crack parameters are shown in the brackets in Table 2. Compared the results of Cases S1 and S2, it indicates that the signal accounted the mode-conversion effect provides additional crack information, and hence, it enables more accurate crack identification.

[Table 2. Sample means and c.o.v.s of crack parameters calculated using TMCMC samples for Cases S1-S3 (error of the identified crack parameters are shown in the bracket)]

[Figure 5. Signal measured at excitation location for Case S3, incident wave: A_0 GW, a) out-of-plane, and b) in-plane displacement measurement]

[Figure 6. Signal measured at excitation location for Case S4, incident wave: S_0 GW, a) in-plane, and b) out-of-plane displacement measurement]

The accuracy of the crack identification utilising A_0 GW (Case S3) and S_0 GW (Case S4) as excitation signal was investigated. Figure 5 shows the SFE simulated GW signals used in Case S3, in which the incident wave is A_0 GW. Figures 5a and 5b show the out-of-plane and in-plane measurement, respectively. Similarly Figure 6 shows the

simulated GW signal of Case S4. The indicate wave is S_0 in Case S4. Figures 6a and 6b show the in-plane and out-of-plane measurement, respectively. Both Cases S3 and S4 consider the mode conversion effect. Figures 5 and 6 show that the mode converted signals provide additional information of the cracks. The results in Table 2 show that the crack parameters are identified accurately in both Cases S3 and S4. In generally, the case using the incident A_0 GW (Case S3) has better performance than the case using incident S_0 GW (Case S4). Comparing the results of the Cracks 1 and 2, the error and c.o.v. of the identified location, width and depth of Crack 2 are small than that of Crack 1. This is because the width and depth of Crack 2 are smaller than Crack 1, and hence, the amplitude of the scattered waves from Crack 2 is smaller than that from Crack 1. Based on the aforementioned findings, the use of incident A_0 GW with both in-plane and out-of-plane measurements could provide better accuracy in identifying the crack parameters. Hence, the rest of the numerical case studies use the A_0 GW as the incident wave signal and both in-plane and out-of-plane data as the measurements.

5.2 Multiple cracks identification

In this section the capability of the proposed multiple crack identification method in determining the number, locations, widths and depths of the cracks is investigated. Three cases (Cases D1, D2 and D3 as shown in Table 1) with different number of cracks and crack parameters for multiple damage identification are considered in this section. Four SFE model classes $M_j, j = 1,...,4$ were considered in each case, where the subscript j denotes the number of cracks in the model class.

The identified number of cracks is presented in Table 3. The table shows the log-likelihood, information gain, log-evidence factor and probability of model classes.

The log-likelihood factor shows the ability of the model class in fitting the measurement. It increase when the complexity of the model class increase (beam with more cracks). The results in Table 3 shows that the log-likelihood factor increases with the model complexity, and hence, it is not possible to determine the crack number based on the log-likelihood factor only. However, the information gain factor also increases with the model complexity, which penalises the complexity of the model class in the log-evidence factor. Hence, the log-evidence factor can be used to determine the optimal modal class, i.e. the number of cracks in the beam. As shown in Table 3, the probability of the model classes is also calculated from the log-evidence and it is closed to 1 for the correct model class (i.e. correct number of cracks) in each case.

The identified crack parameters for each case are summarised in Table 4. It is found that the performance of the TMCMC sampler is reliable in each case as the errors and the c.o.v.s of the identified results are reasonably small. It is also found that TMCMC algorithm is robust in term of the dimension of crack parameters as the c.o.v. of the identified results increases slightly from Cases D1 to D3. Table 4 also shows that Crack 3 in Case D3 has the smallest crack depth and width, and hence, the corresponding identified crack parameters have largest value c.o.v. This indicates that the accuracy of identifying the crack size will decrease when the crack becomes smaller. One possible solution to further improve the crack identification results is to use A_0 GW with shorter wavelength as it is more sensitive to smaller cracks. This can be achieved by increasing the frequency of the excitation signal in practice.

[Table 3. Bayesian model class selection results of Cases D1- D3]

[Table 4. Sample means and c.o.v.s of crack parameters calculated using TMCMC samples for Cases D1-D3 (error of the identified crack parameters are shown in the bracket)]

The evolution of the TMCMC samples of the width of Cracks 1 and 1 at different stages in Case D2 is shown in Figure 7. When the stage number increases, the TMCMC samples converge to the target PDF quickly and finally concentrate in the global optimal region. This shows that the proposed Bayesian approach with TMCMC sampler is efficient in crack identification. Figure 8 shows the posterior marginal PDFs calculated by kernel density estimation (Equation (28)) based on the set of samples in the final stage of the TMCMC sampling as shown in Figure 7. Comparing the posterior marginal PDFs shown in Figure 8, the drop in PDF value away from the peak for the width in Crack 1 is much faster than that for Crack 2. This implies that the uncertainty of the identified width of Crack 2 is higher than that of Crack 1 and this is consistent with the c.o.v.s in Table 4.

[Figure 7. Evolution of the TMCMC samples for the width of Crack 1 and Crack 2 in Case D2]

[Figure 8. Posterior marginal PDFs for the width of Crack 1 and Crack 2 in Case D2]

5.3 Influence of noise level

This section investigates the robustness of the proposed Bayesian approach under different measurement noise levels. Three cases (i.e. Cases N1, N2 and N3) with increasing level of measurement noise (0%, 3% to 6% of the RMS of the measured signal) are considered. The results in Table 5 shows that the numbers of cracks in all cases are correct identified under different measurement noise levels. The probability of model class with the correct number of cracks is prominent (i.e., almost equals to 1) for the Cases N1 and N2, in which measurement noise level 0% and 3% are considered. However, the probability of the optimal model class drops to 0.832 for the measurement

noise level 6%. The sample means and sample c.o.v.s of the crack parameters are shown in Table 6. The results show that errors and c.o.v.s increase with the measurement noise level. Specifically, the c.o.v. of the smaller crack (Crack 2) increases notably in the case of the 6% measurement noise level. This indicates that measurement noise increases the uncertainties in the crack identification.

[Table 5. Bayesian model class selection results for Cases N1-N3]

[Table 6. Sample means and c.o.v.s of crack parameters calculated using TMCMC samples for Cases N1-N3 (the error of the identified crack parameters are shown in the bracket)]

5.4 Influence of crack location

This section investigates the influence of the location of the crack in the proposed Bayesian crack identification method. Two damage cases (Cases L1 and L2) considering two cracks are studied in this section. The details of the cracks are summarised in Table 1. The location of Crack 2 is the same in both cases while the location of Crack 1 in Case L2 is closer to the measurement position (left beam end) than that in Case L1.

[Table 7. Bayesian model class selection results for Cases L1 and L2]

[Table 8. Sample means and c.o.v.s of crack parameters calculated using TMCMC samples for Cases L1 and L2 (error of the identified crack parameters are shown in the bracket)]

The identified crack number is shown in Table 7 and the proposed method correctly identifies the number of cracks based on the probability of the model class.

The sample means and sample c.o.v.s of the crack parameters are summarised in Table 9. The results show that the identified crack parameters for Crack 1 has smaller errors and sample c.o.v.s in Case L2 than in Case L1. This is because Crack 1 is closer to the measurement point in Case L2, and hence, there are more reflected wave pulses from the Crack 1 than that in Case L1 as shown in Figure 9. Figures 9a and 9b show the GW data in out-of-plane and in-plane direction for Cases L1 and L2, respectively, in which Figure 9a is zoomed-in to focus on the reflected wave pulses only for the out-of-plane GW data.

[Figure 9. Signal measured at excitation location for Cases a) L1 and b) L2]

6 Experimental case studies

6.1 Experimental setup

Two aluminium beams (Grade 6060-T5) with length 500 mm, width 12 mm and depth 6 mm were utilised to experimentally demonstrate the effectiveness of the proposed Bayesian multiple cracks identification method. The experimental setup is shown in Figure 10. As shown in Figure 11, a 12×6×2 mm^3 rectangular PZT was bonded to the surface at the left end of each beam using the silver loaded epoxy adhesive. A 12×6×4 mm^3 brass mass was attached on the top of the PZT to increase the excitability of the GW. The excitation signal is a narrow-band 7.5-cycle sinusoidal tone burst modulated by a Hanning window. The excitation signal was synthetised by a central computer and generated by a junction box with maximal 10V output voltage. It was then amplified to the voltage ranged from 10-50V using a signal amplifier (SERVO AMP). Afterward, this amplified signal was applied to the piezoceramic transducer installed on the beam to excite the GW at the left end of the beam.

[Figure 10. Schematic diagram of the experimental setup]

The response displacement was recorded using a 1D laser Doppler vibrometer (PSV-400) head with Laser controller (OFV5000), and hence, only the out-of-plane displacement can be measured in the experiment. Signal averaging and band-pass filter were used to reduce the noise from environmental influence. The measured GW signal data was finally transferred back to the central computer through the data acquisition unit. The measurement location was chosen at 50 mm from the left beam end as shown in Figure 11. For measuring the A_0 GW, the laser measurement position was located at the centre of the longer side of the beam cross-section as shown in Figure 11a. For the S_0 GW the laser measurement position was located at the shorter side of the beam cross-section, and hence, the S_0 GW can be measured through the out-of-plane motion due to the Poisson effect [7]. The cracks were manufactured in the aluminium beams using electric drill, which produced a tolerance of ±1 mm for the crack location and ±0.5 mm for the crack depth and width. The locations and cracks manufactured in the beams are shown in Figure 12.

[Figure 11. Installed piezoceramic transducers and measurement locations in Cases E1-E3 for measuring a) A_0 and b) S_0 incident wave]

[Figure 12. a) The crack in a) Cases E1 and E2 and b) the Cracks 1 and 2 in Case E3]

6.2 Experimental results and discussions

The proposed SFE model with GW mode conversion effect was used to simulate the

numerical data for identifying the cracks in the beams. Cases E1, E2 and E3 were conducted to experimentally verify the proposed multiple cracks identification method. Case E1 used S_0 mode GW as the excitation signal while Case E2 employed A_0 GW. The excitation frequency was 80 kHz and a single crack was considered in both cases. Case E3 considered two cracks in the beam and the excited signal was a 110 kHz A_0 GW.

The identified numbers of cracks are summarised in Table 9. It is shown that the crack number is correctly identified and the probability of the correct crack number is closed to 1 in all cases. This proves that the proposed Bayesian approach is able to identify the correct number of cracks in practice situation. The sample means and sample c.o.v.s of the identified crack parameters are shown in Table 10. For Cases E1 and E2, the identified crack parameters and corresponding sample c.o.v.s are compared to determine a suitable excitation GW signal. Specifically, it is found that the Case E2 using A_0 GW as the incident wave has smaller errors and sample c.o.v.s than Case E1, in which S_0 GW is used as the incident wave. This experimentally confirms that using A_0 GW as the incident wave is superior to using S_0 GW as the incident wave in identifying small cracks, i.e. Crack 2. The sample c.o.v. of the identified crack parameters increases as the smaller amplitude of the GW reflected from the crack with smaller size, and hence, less information is available for the crack identification. To illustrate how well the simulated signals, which is calculated by the SFT beam model with the identified crack parameters, matches the experimental results, a comparison between the simulated and measured time-domain response for Cases E1, E2 and E3 are shown in Figure 13.

[Table 9. Bayesian model class selection result for Cases E1-E3]

[Table 10. Sample means and c.o.v.s of crack parameters calculated using TMCMC samples for Cases E1-E3 (error of the identified crack parameters are shown in the bracket)]

[Figure 13. Comparison of the simulated and measured time-domain GW signals for Cases a) E1, b) E2 and c) E3]

7 Conclusions

In this paper the GW Bayesian identification of multiple cracks using TMCMC algorithm in beams has been presented. This study has extended the crack identification using GW model based approach to identify the number of cracks and the crack parameters (i.e., crack location, depth and width). The time-domain SFE method based on Mindlin-Herrmann rod and Timoshenko beam theory has been presented and a spectral cracked beam element simulating the mode conversion effect when the GW interacting with the cracks has been proposed for crack identification.

Numerical case studies have been conducted to study the performance of different GW modes in identifying the crack parameters. Also, the influences of mode conversion effect, measurement noise level and distance between the cracks and the excitation location on the accuracy of the crack identification results have been investigated in detail. The uncertainties associated with the identified crack parameters have been indicated by the sample c.o.v.s of the identified crack parameters. It is found that the A_0 GW performs better than S_0 GW as the sample c.o.v.s of the identified crack parameters is smaller, which shows that the A_0 GW is more sensitive for identifying the cracks with smaller sizes. Furthermore, it has demonstrated that the proposed Bayesian approach is robust to the different measurement noise and location. The findings have indicated that the use of the mode conversion effect could effectively improve the accuracy of the

crack identification.

Different crack scenarios have been studied numerically to investigate the performance of the proposed Bayesian multiple cracks identification method. The Bayesian model class selection method has been used to determine the number of the cracks and the uncertainties of identified crack parameters have been indicated by the sample c.o.v.s of the crack parameters. The results are encouraging as the number of crack and the crack parameters in each scenario have been accurately identified. Finally, this Bayesian damage identification algorithm has been experimentally verified to demonstrate the practicability of the proposed method.

Acknowledgements

The work was supported by the Australian Research Council under grant number DE130100261. The support is greatly appreciated.

Appendix A

This appendix presents the details of the F_I, F_{II} and H required for calculating the I_{c1}, I_{c2}, I_{c3} and I_{c4} in Equation (21). The details of derivations can be found in [47] and [48]. The F_I and F_{II} shown in Equation (21) are defined as

$$F_I = \left[\gamma_1 + \gamma_2 \left(\frac{d_c}{h} \right)^2 + \gamma_3 \left(\frac{d_c}{h} \right)^4 \right] f_\phi g f_w \tag{32}$$

$$F_{II} = \frac{\beta (d_c/h) \cos\phi}{B_1 \left[\sin^2\phi + (d_c/h)^2 \cos^2\phi \right]^{1/4}} \tag{33}$$

where $\beta = 1 - \kappa^2$,

$$B_1 = (\beta - \nu)\int_0^{\pi/2} \sqrt{1-\beta\sin^2\phi}\, d\phi + \nu\kappa \int_0^{\pi/2} \frac{1}{\sqrt{1-\beta\sin^2\phi}}\, d\phi \tag{34}$$

$$\gamma_1 = 1.13 - 0.09\kappa \tag{35}$$

$$\gamma_2 = -0.54 + \frac{0.89}{0.2+\kappa} \tag{36}$$

$$\gamma_3 = -0.5 - \frac{1.0}{0.65+\kappa} + 14\left(1.0-\kappa\right)^{24} \tag{37}$$

$$g = 1 + \left[0.1 + 0.35\left(\frac{d_c}{h}\right)^2\right]\left(1-\sin\phi\right)^2 \tag{38}$$

The angular function f_ϕ for the half elliptical crack in F_I is

$$f_\phi = \left[\kappa^2\cos^2\phi + \sin^2\phi\right]^{1/4} \tag{39}$$

The finite width calibrated function f_w is

$$f_w = \left[\sec\left(\frac{\pi b_c}{4b}\sqrt{\frac{d_c}{h}}\right)\right]^{1/2} \tag{40}$$

The function F_I is the boundary-correction factor for tension. The product of H and F_I shown in Equation (21) is the boundary-calibration factor for bending, where H is expressed

$$H = H_1 + \left(H_2 - H_1\right)\left(\sin\phi\right)^{\left(0.2+\kappa+\frac{0.6d_c}{h}\right)} \tag{41}$$

where

$$H_1 = 1 - 0.34\frac{d_c}{h} - 0.11\kappa\left(\frac{d_c}{h}\right) \text{ and } H_2 = 1 - G_1\left(\frac{d_c}{h}\right) + G_2\left(\frac{d_c}{h}\right)^2 \tag{42}$$

$$G_1 = 1.22 + 0.12\kappa \text{ and } G_2 = 0.55 - 1.05\kappa^{0.75} + 0.47\kappa^{1.5} \tag{43}$$

References

[1] D. Aljets, A. Chong, S. Wilcox, K. Holford, Acoustic emission source location on large plate-like structures using a local triangular sensor array, Mechanical Systems and Signal Processing, 30 (2012) 91-102.

[2] A.A. Mosavi, D. Dickey, R. Seracino, S. Rizkalla, Identifying damage locations under ambient vibrations utilizing vector autoregressive models and Mahalanobis distances, Mechanical systems and signal processing, 26 (2012) 254-267.

[3] A. Raghavan, C.E.S. Cesnik, Review of Guided-wave Structural Health Monitoring, The Shock and Vibration Digest, 39 (2007) 91-114.

[4] A.J. Croxford, P.D. Wilcox, B.W. Drinkwater, G. Konstantinidis, Strategies for guided-wave structural health monitoring, Proceedings of the Royal Society, 463 (2007) 2961-2981.

[5] W. Zhou, H. Li, F.G. Yuan, Guided wave generation, sensing and damage detection using in-plane shear piezoelectric wafers, Smart Materials and Structures, 23 (2014) 015014.

[6] M.J. Lowe, P. Cawley, A. Galvagni, Monitoring of corrosion in pipelines using guided waves and permanently installed transducers, The Journal of the Acoustical Society of America, 132 (2012) 1932-1932.

[7] C.T. Ng, Bayesian model updating approach for experimental identification of damage in beams using guided waves, Structural Health Monitoring, (2014) 1475921714532990.

[8] C.T. Ng, On the selection of advanced signal processing techniques for guided wae damage identification using a statistical approach, Engineering Structures, 67 (2014) 50-60.

[9] C.T. Ng, On Accuracy of Analytical Modeling of Lamb Wave Scattering at Delaminations in Multilayered Isotropic Plates, International Journal of Structural Stability and Dynamics, 15 (2015) 1540010.

[10] C.R. Farrar, K. Worden, An introduction to structural health monitoring, Philosophical Transactions of the Royal Society A: Mathematical, Physical and Engineering Sciences, 365 (2007) 303-315.

[11] M. Veidt, C.T. Ng, S. Hames, T. Wattinger, Imaging Laminar Damage in Plates Using Lamb Wave Beamforming, Advanced Materials Research, 47-50 (2008) 666-669.

[12] C.T. Ng, M. Veidt, N. Rajic, Integrated Piezoceramic Transducers for Imaging Damage in Composite Laminates, In Proceeding of SPIE (The 2nd International Conference on Smart Materials and Nanotechnology in Engineering), Weihai, China, 2009, pp. 74932M-74931-74938.

[13] E.B. Flynn, M.D. Todd, P.D. Wilcox, B.W. Drinkwater, A.J. Croxford,

Maximum-likelihood estimation of damage location in guided-wave structural health monitoring, Proceedings of the Royal Society of London A: Mathematical, Physical and Engineering Sciences, The Royal Society, 2011, pp. rspa20110095.

[14] C.T. Ng, A two-stage approach for quantitative damage imaging in metallic plates using Lamb waves, Earthqu. Struct., 8 (2015) 821-841.

[15] L.F. Rose, C.H. Wang, Mindlin plate theory for damage detection: imaging of flexural inhomogeneities, The Journal of the Acoustical Society of America, 127 (2010) 754-763.

[16] J.H. Han, Y.-J. Kim, Time–frequency beamforming for nondestructive evaluations of plate using ultrasonic Lamb wave, Mechanical Systems and Signal Processing, 54 (2015) 336-356.

[17] O.A. Vanli, S. Jung, Statistical updating of finite element model with Lamb wave sensing data for damage detection problems, Mechanical Systems and Signal Processing, 42 (2014) 137-151.

[18] P. Aryan, A. Kotousov, C.T. Ng, A model-based method for damage detection with guided waves, Strucutral Control & Health Montiroing, (2016) doi:10.1002/stc.1884.

[19] E.B. Flynn, M.D. Todd, A.J. Croxford, B.W. Drinkwater, P.D. Wilcox, Enhanced detection through low-order stochastic modeling for guided-wave structural health monitoring, Structural Health Monitoring, (2011) 1475921711414232.

[20] J. Yang, J. He, X. Guan, D. Wang, H. Chen, W. Zhang, Y. Liu, A probabilistic crack size quantification method using in-situ Lamb wave test and Bayesian updating, Mechanical Systems and Signal Processing, (2015).

[21] M. Rucka, Experimental and numerical studies of guided wave damage detection in bars with structural discontinuities, Archive of Applied Mechanics, 80 (2010) 1371-1390.

[22] H.Z. Hossein Abadi, R. Amirfattahi, B. Nazari, H.R. Mirdamadi, S.A. Atashipour, GUW-based structural damage detection using WPT statistical features and multiclass SVM, Applied Acoustics, 86 (2014) 59-70.

[23] U. Amjad, S.K. Yadav, T. Kundu, Detection and quantification of pipe damage from change in time of flight and phase, Ultrasonics, 62 (2015) 223-236.

[24] C. Willberg, S. Duczek, J. Vivar-Perez, Z. Ahmad, Simulation Methods for Guided Wave-Based Structural Health Monitoring: A Review, Applied Mechanics Reviews, 67 (2015) 010803.

[25] W.J. Zhou, M.N. Ichchou, Wave scattering by local defect in structural waveguide through wave finite element method, Structural Health Monitoring, 10 (2011) 335-349.

[26] F. Xu, Y. Zhang, W. Hong, K. Wu, T.J. Cui, Finite-difference frequency-domain algorithm for modeling guided-wave properties of substrate integrated waveguide,

Microwave Theory and Techniques, IEEE Transactions on, 51 (2003) 2221-2227.
[27] A. Bergamini, F. Biondini, Finite strip modeling for optimal design of prestressed folded plate structures, Engineering Structures, 26 (2004) 1043-1054.
[28] X.G. Zhao, J.L. Rose, Boundary element modeling for defect characterization potential in a wave guide, International Journal of Solids and Structures, 40 (2003) 2645-2658.
[29] M. Krawczuk, Application of spectral beam finite element with a crack and iterative search technique for damage detection, Finite Elements in Analysis and Design, 38 (2002) 537-548.
[30] A. Nag, D. Roy Mahapatra, S. Gopalakrishnan, Identification of Delamination in Composite Beams using Spectral Estimation and a Genetic Algorithm, Smart Materials and Structures, 11 (2002) 899-908.
[31] C.T. Ng, M. Veidt, H.F. Lam, Guided Wave Damage Characterisation in Beams Utilising Probabilistic Optimisation, Engineering Structures, 31 (2009) 2842-2850.
[32] A.T. Patera, A spectral element method for fluid dynamics: laminar flow in a channel expansion, Journal of Computational Physics, 54 (1984) 468-488.
[33] C. Pozrikidis, Introduction to finite and spectral element methods using Matlab, CRC Press, 2005.
[34] P. Kudela, M. Krawczuk, W. Ostachowicz, Wave propagation modelling in 1D structures using spectral finite elements, Journal of Sound and Vibration, 300 (2007) 88-100.
[35] R. Mindlin, G. Herrmann, A one-dimensional theory of compressional waves in an elastic rod, Proceedings of the 1st US National Congress of Applied Mechanics, 1951, pp. 187-191.
[36] J.F. Doyle, Wave propagation in structures, Springer, 1989.
[37] K. Xu, D. Ta, Z. Su, W. Wang, Transmission analysis of ultrasonic Lamb mode-conversion in a plate with partial-thickness notch, Ultrasonics, 54 (2014) 395-401.
[38] F. Li, X. Sun, J. Qiu, L. Zhou, H. Li, G. Meng, Guided wave propagation in high-speed train axle and damage detection based on wave mode-conversion, Structural Control and Health Monitoring, (2015).
[39] S. He, C.T. Ng, Analysis of mode-conversion and scattering of guided waves at cracks in isotropic beams using a time-domain spectral finite element method, Electron. Journal of Structural Engineering., 14 (2015) 20-32.
[40] J.L. Beck, L.S. Katafygiotis, Updating Models and Their Uncertainties I: Bayesian Statistical Framework, Journal of Engineering Mechanics, ASCE, 124 (1998) 455-461.
[41] J.L. Beck, K.V. Yuen, Model selection using response measurements: Bayesian probabilistic approach, Journal of Engineering Mechanics, 130 (2004) 192-203.

[42] J.L. Beck, Bayesian system identification based on probability logic, Structural Control and Health Monitoring, 17 (2010) 825-847.

[43] J. Ching, Y.C. Chen, Transitional Markov chain Monte Carlo method for Bayesian model updating, model class selection, and model averaging, Journal of Engineering Mechanics, 133 (2007) 816-832.

[44] M. Krawczuk, J. Grabowska, M. Palacz, Longitudinal wave propagation Part I - Comparison of rod theories, Journal of Sound and Vibration, 295 (2006) 461-478.

[45] G.R. Irwin, Crack-extension force for a part-through crack in a plate, Journal of Applied Mechanics, 29 (1962) 651-654.

[46] A. Darpe, K. Gupta, A. Chawla, Coupled bending, longitudinal and torsional vibrations of a cracked rotor, Journal of Sound and Vibration, 269 (2004) 33-60.

[47] J.C. Newman, I. Raju, An empirical stress-intensity factor equation for the surface crack, Engineering Fracture Mechanics, 15 (1981) 185-192.

[48] M. He, J. Hutchinson, Surface crack subject to mixed mode loading, Engineering Fracture Mechanics, 65 (2000) 1-14.

[49] S.K. Au, F.A. DiazDelaO, I. Yoshida, Bayesian updating and model class selection with Subset Simulation, arXiv preprint arXiv:1510.06989, (2015).

[50] M.K. Vakilzadeh, Y. Huang, J.L. Beck, T. Abrahamsson, Approximate Bayesian Computation by Subset simulation using hierarchical state-space models, Mechanical Systems and Signal Processing (2016) doi:10.1016/j.ymssp.2016.02.024.

[51] D. Straub, I. Papaioannou, Bayesian updating with structural reliability methods, Journal of Engineering Mechanics, ASCE 141(3) (2015) 0.4014134.

[52] M. Muto, J.L. Beck, Bayesian updating and model class selection for hysteretic structural models using stochastic simulation, Journal of Vibration and Control, 14 (2008) 7-34.

[53] S.F. Gull, Bayesian inductive inference and maximum entropy, Maximum-entropy and Bayesian methods in science and engineering, Springer, 1988, pp. 53-74.

[54] J.M. Nichols, W.A. Link, K.D. Murphy, C.C. Olson, A Bayesian approach to identifying structural nonlinearity using free-decay response: Application to damage detection in composites, Journal of Sound and Vibration, 329 (2010) 2995-3007.

[55] S.K. Au, J.L. Beck, A new adaptive importance sampling scheme, Structural Safety, 21 (1999) 135-158.

[56] H.F. Lam, Y. Yang, S.K. Au, Bayesian model updating of a coupled-slab system using field test data utilizing an enhanced Markov chain Monte Carlo simulation algorithm, Engineering Structures, 102 (2015) 144-155.

TABLE LIST

Table 1: Summary of all numerical and experimental case studies

Scenario		Numerical case studies											Experimental case studies		
		GW mode selection				Multiple cracks identification			Measurement noise influence			Crack location effect				
Damage case		S1	S2	S3	S4	D1	D2	D3	N1	N2	N3	L1	L2	E1	E2	E3
Incident wave		A_0			S_0	A_0			A_0			A_0		S_0	A_0	
Measurement direction*		*y*-dir.		*x*-dir. & *y*-dir.		*x*-dir. & *y*-dir.			*x*-dir. & *y*-dir.			*x*-dir. & *y*-dir.		*z*-dir.#	*y*-dir.	
Mode conversion effect		N	Y			Y			Y			Y		Y		
Measurement noise (%)		3				3			0	3	6	3		3		
Crack number		2				1	2	3	2			2		1	2	
Crack 1 (mm)	L_c	200				250	200		200			200	100	250±1	200±1	
	d_c	3				3		2	3			3		3±0.5		
	b_c	6				6			6			6		6±0.5		
Crack 2 (mm)	L_c	350					350	300	350			350			350±1	
	d_c	2					2	3	2			2			2±0.5	
	b_c	5					5	6	5			5			5±0.5	
Crack 3 (mm)	L_c							400								
	d_c							2								
	b_c							4								

* The measurement direction is consistent with the coordinate system in Fig. 2.

The S_0 is measured from *z*-dir. through the Poisson's effect in experiment.

L_c = crack location, d_c = crack depth, b_c = crack width.

Table 2: Sample means and c.o.v.s of crack parameters calculated using TMCMC samples for Cases S1-S3 (errors of the identified crack parameters are shown in the bracket)

Case		Crack1 (mm)			Crack 2 (mm)		
		L_c	d_c	b_c	L_c	d_c	b_c
	Actual	200	3	6	350	2	5
S1	Sample mean	200.21 (0.11%)	2.73 (8.97%)	5.91 (1.53%)	350.51 (0.15%)	1.62 (19.15%)	5.40 (7.96%)
	Sample c.o.v (%)	0.0446	0.3749	0.3193	0.0352	6.7854	4.1015
S2	Sample mean	200.12 (0.06%)	2.84 (5.33%)	5.98 (0.33%)	350.31 (0.09%)	1.80 (9.85%)	5.19 (3.79%)
	Sample c.o.v (%)	0.0175	0.2142	0.1299	0.0258	4.5132	3.0037
S3	Sample mean	200.03 (0.02%)	2.99 (0.08%)	5.99 (0.07%)	350.02 (0.01%)	2.01 (0.05%)	4.79 (4.17%)
	Sample c.o.v (%)	0.0016	0.2196	0.1153	0.0157	0.3367	0.1534
S4	Sample mean	200.09 (0.05%)	2.99 (0.21%)	5.99 (0.17%)	350.49 (0.14%)	1.90 (4.88%)	5.09 (1.82%)
	Sample c.o.v (%)	0.0331	0.6404	0.3498	0.1550	5.0371	4.4294

Table 3. Bayesian model class selection results of Cases D1-D3

Case	Model class	Log-likelihood	Information gain	Log-evidence	Probability
D1	**M_1**	**3447.43**	**17.08**	**3430.35**	**0.9289**
	M_2	3448.42	20.62	3427.80	0.0711
D2	M_1	3458.31	11.52	3446.79	0
	M_2	**3815.65**	**12.37**	**3803.28**	**0.9998**
	M_3	3816.28	21.28	3795.00	0.0002
D3	M_1	3345.90	11.52	3334.38	0
	M_2	3940.62	29.80	3910.82	0
	M_3	**4160.19**	**65.69**	**4094.50**	**1**
	M_4	4202.60	125.63	4076.97	$2.43e^{-8}$

Table 4. Sample means and c.o.v.s of crack parameters calculated using TMCMC samples for Cases D1-D3 (errors of the identified crack parameters are shown in the bracket)

Case		Crack 1 (mm)			Crack 2 (mm)			Crack 3 (mm)		
		L_c	d_c	b_c	L_c	d_c	b_c	L_c	d_c	b_c
D1	Actual	250	3	6	-	-	-	-	-	-
	Sample mean	250.09 (0.04%)	2.71 (9.67%)	5.99 (0.17%)	-	-	-	-	-	-
	Sample c.o.v (%)	0.0125	0.6450	0.2990	-	-	-	-	-	-
D2	Actual	200	3	6	350	2	5	-	-	-
	Sample mean	200.20 (0.10%)	2.99 (0.07%)	5.71 (4.83%)	350.50 (0.23%)	2.09 (4.50%)	4.99 (0.19%)	-	-	-
	Sample c.o.v (%)	0.0784	0.3251	0.3982	0.0515	1.1788	0.9194	-	-	-
D3	Actual	200	2	6	300	3	6	400	2	4
	Sample mean	200.20 (0.10%)	1.99 (0.49%)	5.90 (1.67%)	300.50 (0.16%)	2.99 (0.07%)	5.99 (0.18%)	401.01 (0.25%)	1.12 (43.51%)	3.13 (21.75%)
	Sample c.o.v (%)	0.0071	0.0330	0.0480	0.0079	0.0250	0.0059	0.0288	1.5149	3.9409

Table 5. Bayesian model class selection results for Cases N1-N3

Case	Model class	Log-likelihood	Information gain	Log-evidence	Probability
N1	M_1	3605.23	10.71	3594.52	0
	M_2	**4156.31**	**21.07**	**4135.24**	**0.9589**
	M_3	4156.75	24.66	4132.09	0.0411
N2	M_1	3458.28	10.52	3447.76	0
	M_2	**3815.82**	**12.37**	**3803.45**	**0.9999**
	M_3	3816.17	22.08	3794.09	0.0001
N3	M_1	3126.59	10.50	3116.09	0
	M_2	**3307.80**	**18.87**	**3288.93**	**0.8468**
	M_3	3309.17	21.95	3287.22	0.1532

Table 6. Sample means and c.o.v.s of crack parameters calculated using TMCMC samples for Cases N1-N3 (errors of the identified crack parameters are shown in the bracket)

Case		Crack 1 (mm)			Crack 2 (mm)		
		L_c	d_c	b_c	L_c	d_c	b_c
	Actual	200	3	6	350	2	5
N1	Sample mean	200.01 (0.01%)	2.99 (0.07%)	5.99 (0.09%)	350.09 (0.03%)	1.97 (1.49%)	4.98 (0.41%)
	Sample c.o.v (%)	0.0015	0.0542	0.0292	0.0126	0.172	0.132
N2	Sample mean	200.5 (0.25%)	2.99 (0.13%)	5.90 (1.67%)	350.81 (0.23%)	1.91 (4.52%)	4.98 (0.40%)
	Sample c.o.v (%)	0.0016	0.2196	0.1153	0.0157	0.3367	0.1534
N3	Sample mean	200.9 (0.45%)	2.99 (0.32%)	5.80 (3.33%)	350.1 (0.03%)	1.89 (5.47%)	5.49 (9.79%)
	Sample c.o.v (%)	0.0106	0.2431	0.1612	0.0234	2.7934	2.4198

Table 7. Bayesian model class selection results for Cases L1 and L2

Case	Model class	Log-likelihood	Information gain	Log-evidence	Probability
L1	M_1	3458.33	10.52	3447.81	0
	M_2	**3815.79**	**12.37**	**3803.42**	**0.9999**
	M_3	3816.21	22.08	3794.13	0.0001
L2	M_1	3602.14	13.30	3588.84	0
	M_2	**4432.05**	**15.14**	**4416.91**	**0.8375**
	M_3	4432.13	16.86	4415.27	0.1625

Table 8. Sample means and c.o.v.s of crack parameters calculated using TMCMC sample for Cases L1 and L2 (errors of the identified crack parameters are shown in the bracket)

Case		Crack 1 (mm)			Crack 2 (mm)		
		L_c	d_c	b_c	L_c	d_c	b_c
L1	Actual	200	3	6	350	2	5
	Sample mean	200.51 (0.26%)	2.99 (0.31%)	5.91 (1.50%)	350.79 (0.23%)	1.90 (5.00%)	4.99 (0.19%)
	Sample c.o.v (%)	0.0274	0.2274	0.2425	0.0499	0.1629	0.1199
L2	Actual	100	3	6	350	2	5
	Sample mean	100.01 (0.01%)	2.99 (0.03%)	5.99 (0.06%)	350.01 (0.01%)	1.98 (0.11%)	4.98 (0.42%)
	Sample c.o.v (%)	0.0210	0.0839	0.0461	0.0655	0.1513	0.0702

Table 9. Bayesian model class selection for the experimental results

Case	Model class	Log-likelihood	Information gain	Log-evidence	Probability
E1	**M_1**	**485.69**	**7.75**	**477.95**	**0.9989**
	M_2	483.80	24.63	471.17	0.0011
E2	**M_1**	**1099.90**	**-6.89**	**1093.01**	**1**
	M_2	1106.21	-24.88	1081.33	8.46e-06
E3	M_1	1050.02	-10.37	1039.65	1.07e-57
	M_2	**1193.21**	**-22.47**	**1170.74**	**0.9183**
	M_3	1203.59	-35.27	1168.32	0.0817

Table 10. Sample means and c.o.v.s of crack parameters calculated using TMCMC sample for Cases E1-E3 (errors of the identified crack parameters are shown in the bracket)

Case		Crack 1 (mm)			Crack 2 (mm)		
		L_c	d_c	b_c	L_c	d_c	b_c
E1	Actual	250	3	6	-	-	-
	Sample mean	260.10 (4.04%)	2.80 (6.67%)	5.71 (4.83%)	-	-	-
	Sample c.o.v (%)	0.0148	0.9735	3.3643	-	-	-
E2	Actual	250	3	6	-	-	-
	Sample mean	250.31 (-0.12%)	2.81 (6.33%)	5.80 (3.33%)	-	-	-
	Sample c.o.v (%)	0.0094	0.2051	1.5048	-	-	-
E3	Actual	200	3	6	350	2	6
	Sample mean	200.53 (0.27%)	2.42 (19.33%)	5.03 (16.17%)	349.92 (0.02%)	1.33 (33.5%)	5.89 (1.83%)
	Sample c.o.v (%)	0.0169	0.3504	0.3389	0.0278	0.6413	0.4152

Figure List

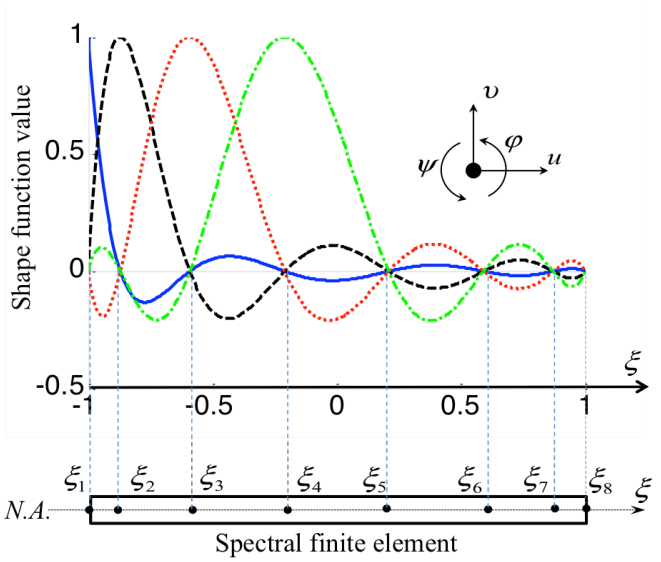

Figure 1. Distribution of GLL nodes and shape function of the first four nodes (1st node: solid line; 2nd node: dashed line; 3rd node: dotted line; 4th node: dotted-dashed line)

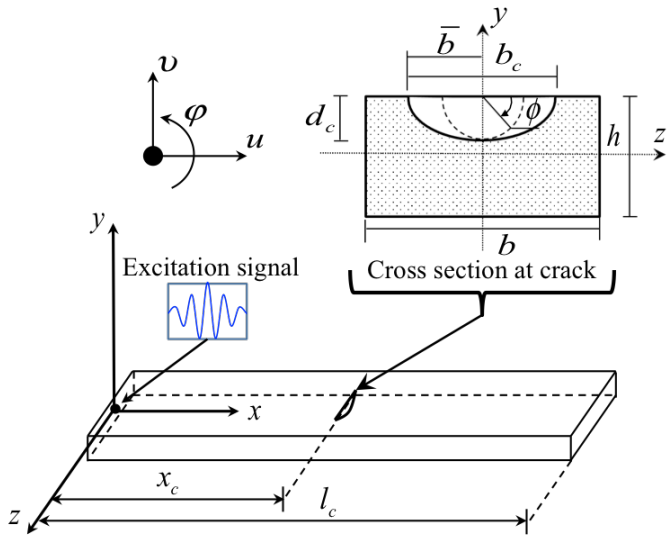

Figure 2. Schematic diagram of the cracked element for simulating a part-through surface crack

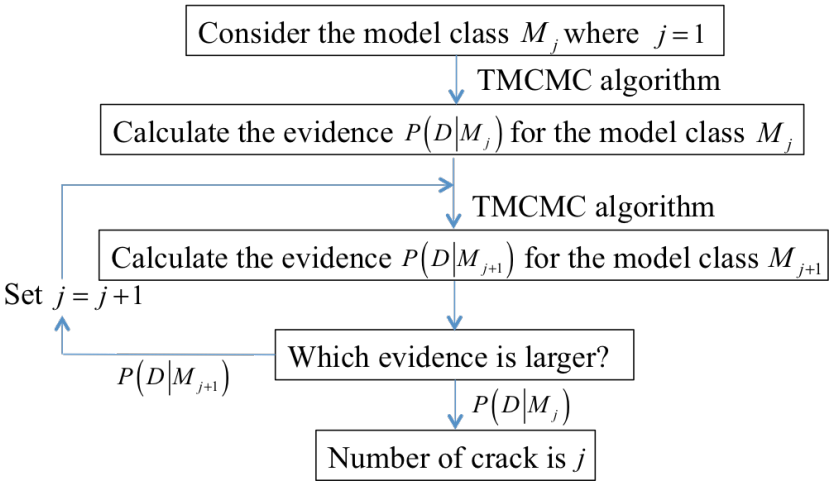

Figure 3. Framework of Bayesian model class selection

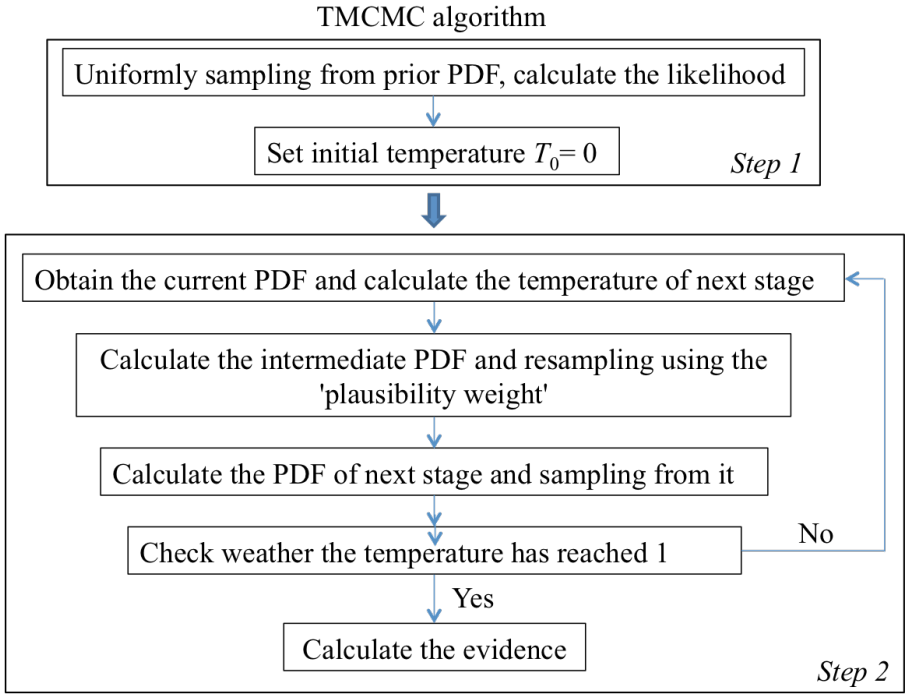

Figure 4. Framework of TMCMC algorithm

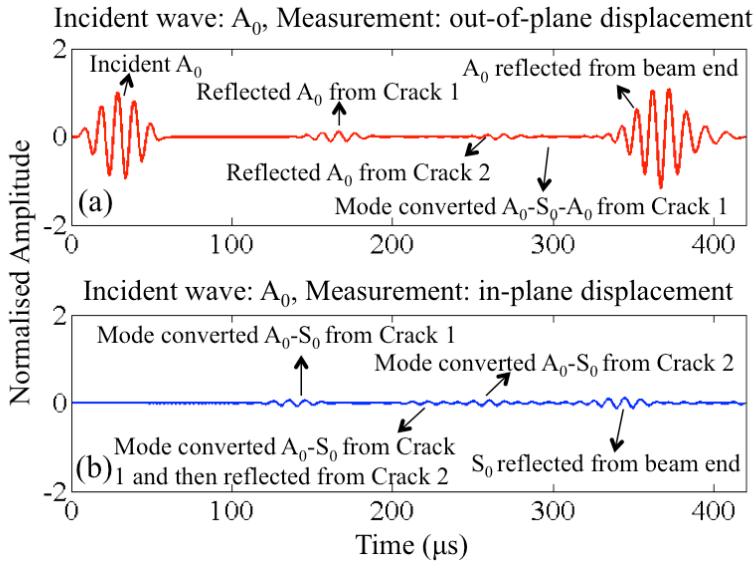

Figure 5. Signal measured at excitation location for Case S3, incident wave: A_0 GW, a) out-of-plane, and b) in-plane displacement measurement

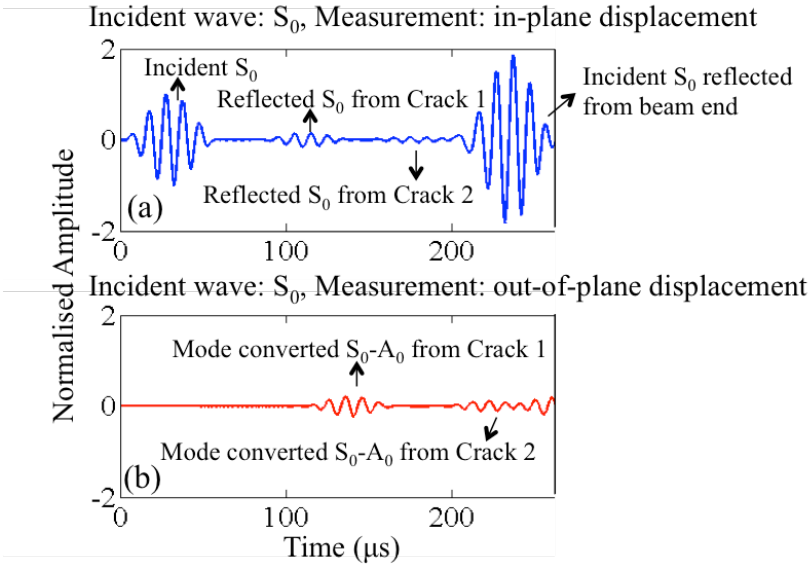

Figure 6. Signal measured at excitation location for Case S4, incident wave: S_0 GW, a) in-plane, and b) out-of-plane displacement measurement

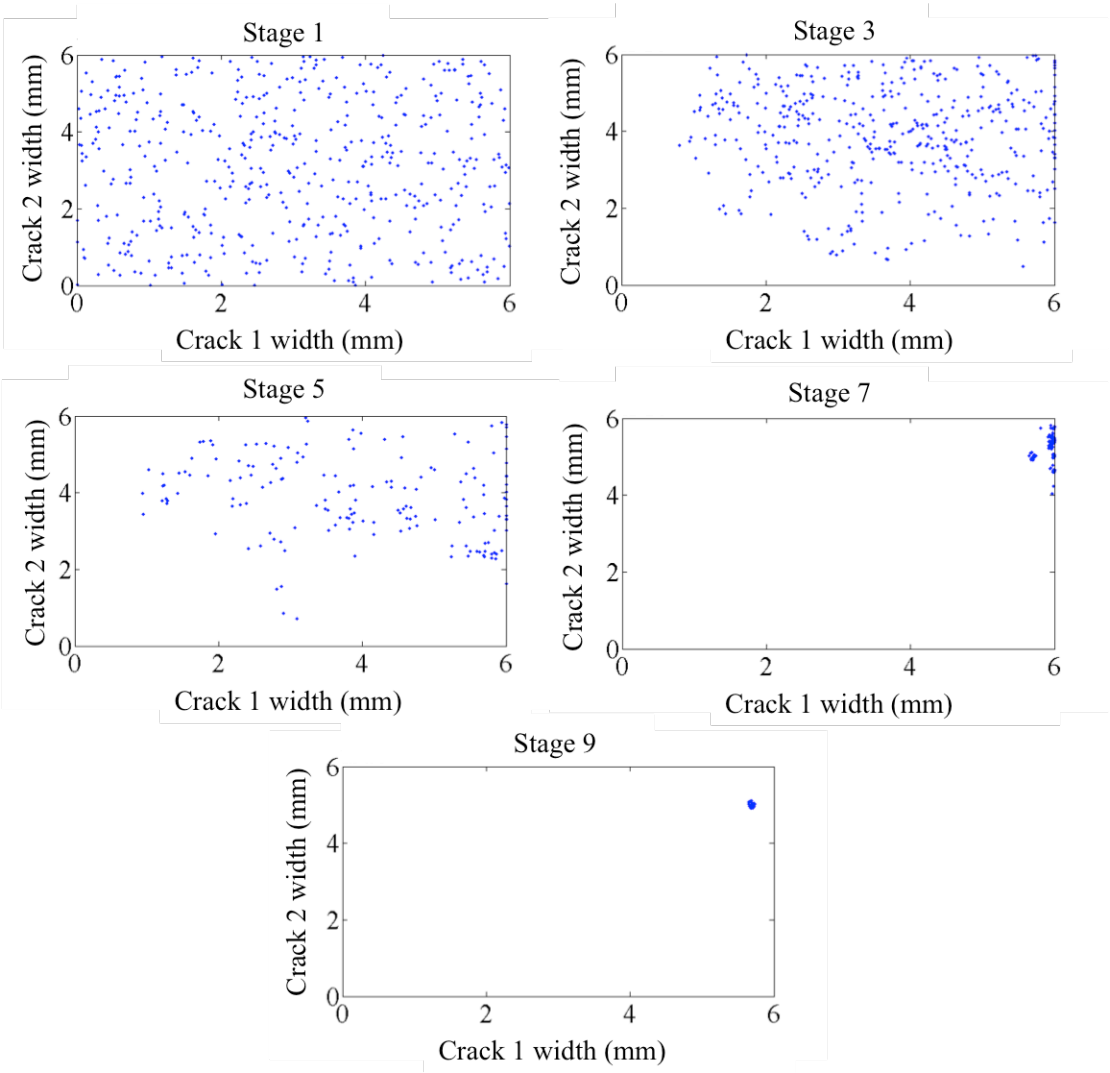

Figure 7. Evolution of the TMCMC samples for the width of Crack 1 and Crack 2 in Case D2

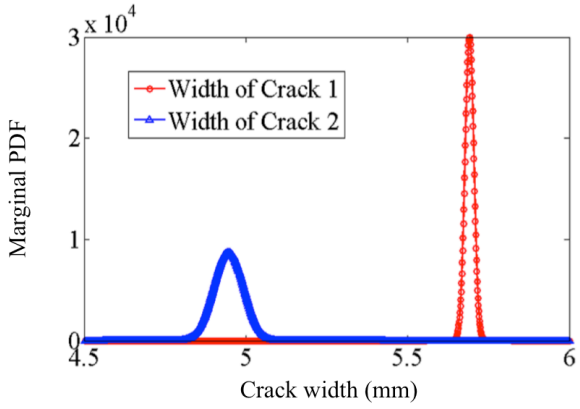

Figure 8. Posterior marginal PDFs for the width of Crack 1 and Crack 2 in Case D2

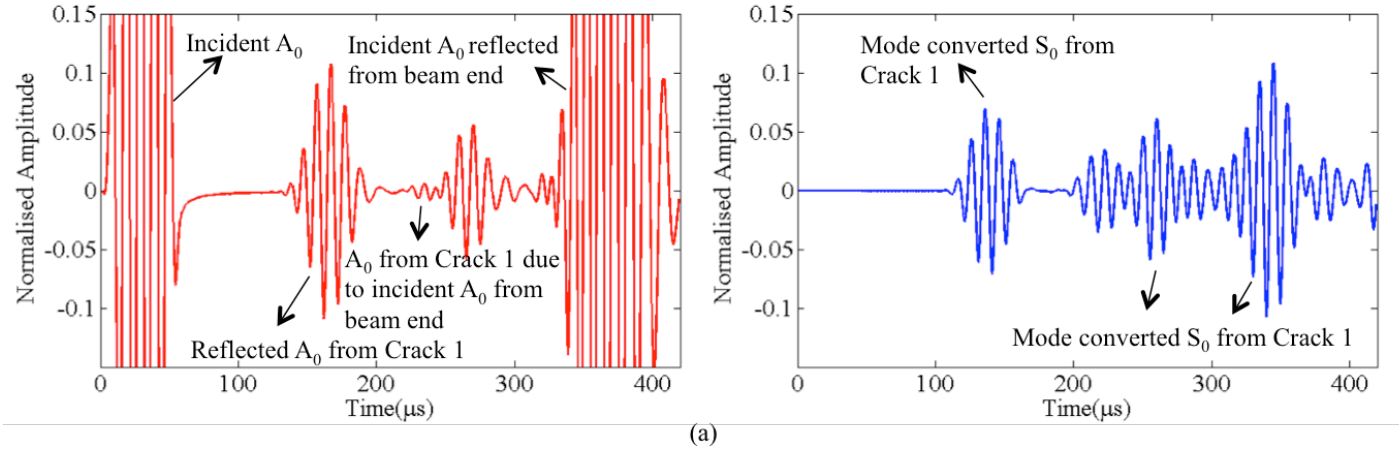

(a)

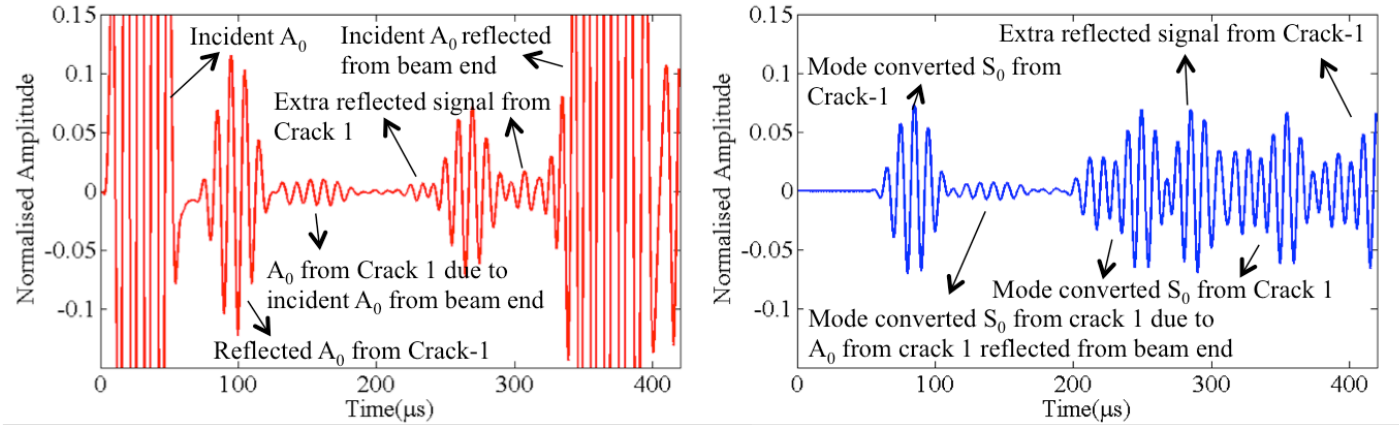

(b)

Figure 9. Signal measured at excitation location for Cases a) L1 and b) L2

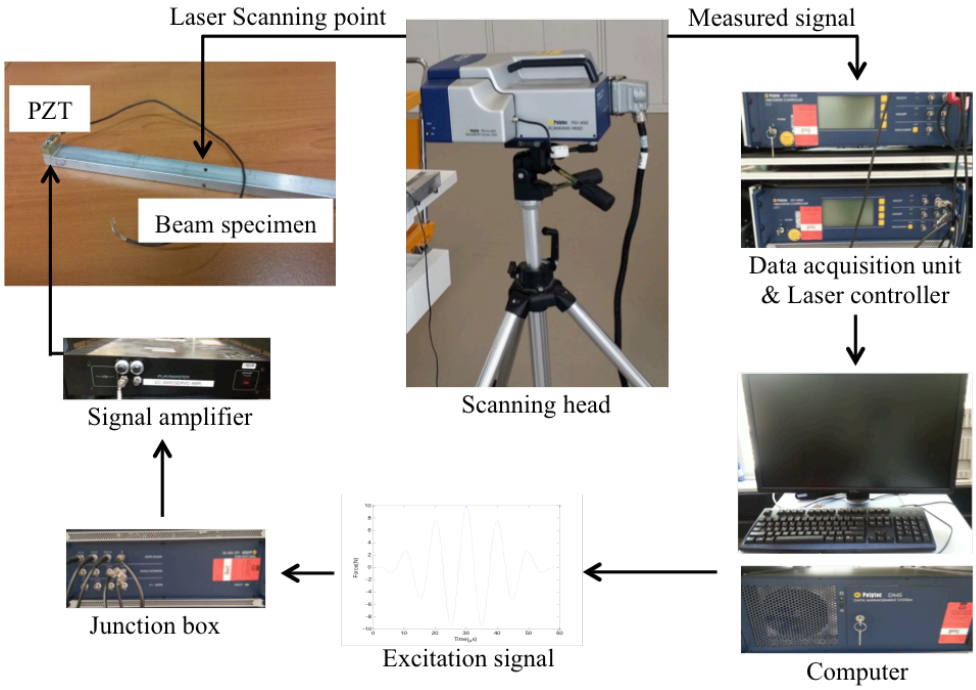

Figure 10. Schematic diagram of the experimental setup

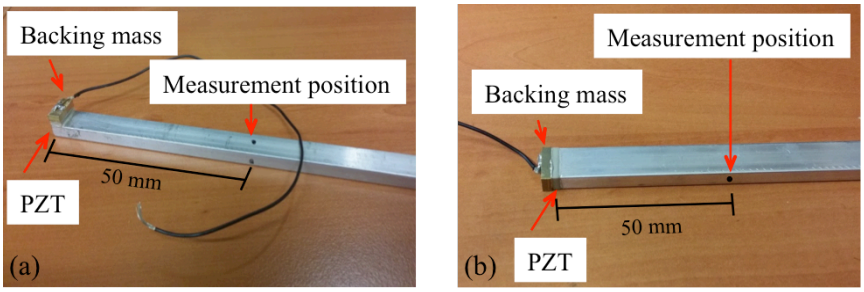

Figure 11. Installed piezoceramic transducers and measurement locations in Cases E1-E3 for measuring a) A_0 and b) S_0 incident wave

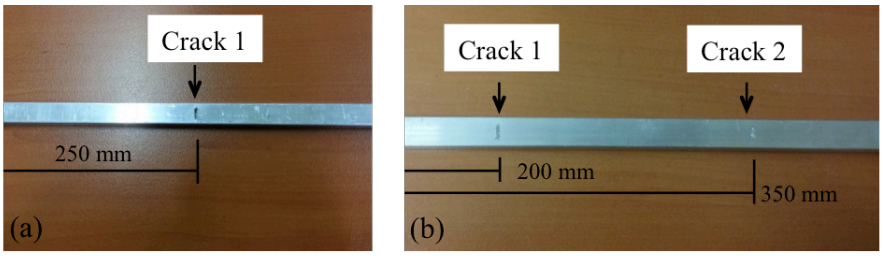

Figure 12. a) The crack in a) Cases E1 and E2 and b) the Cracks 1 and 2 in Case E3

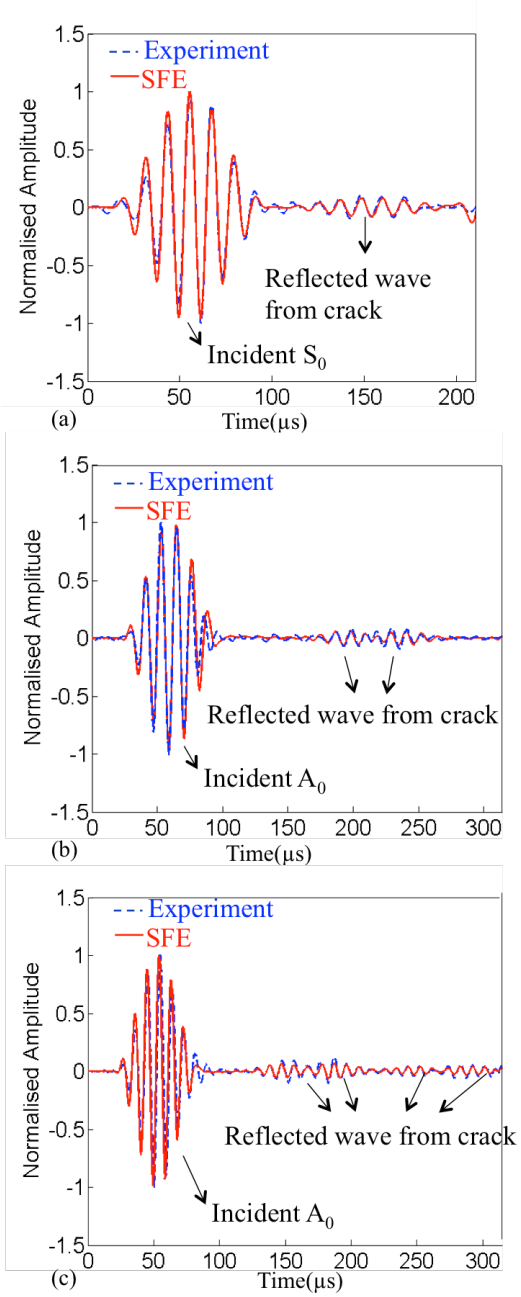

Figure 13. Comparison of the simulated and measured time-domain GW signals for Cases a) E1, b) E2 and c) E3